

Atmospheric Wind Retrievals from Satellite Soundings over the Middle- and High-Latitude Oceans

CHENG-ZHI ZOU AND MICHAEL L. VAN WOERT

Office of Research and Applications, NOAA/NESDIS, Camp Springs, Maryland, and U. S. National Ice Center, Washington, D.C.

(Manuscript received 12 April 2001, in final form 18 December 2001)

ABSTRACT

A technique that uses satellite-based surface wind and temperature soundings for deriving three-dimensional atmospheric wind fields is developed for climate studies over the middle- and high-latitude oceans. In this technique, the thermal wind derived from the satellite soundings is added to the surface wind to obtain a first-guess, nonmass-conserved atmospheric wind profile. Then a Lagrange multiplier in a variational formalism is used to force the first-guess wind to conserve mass. Two mass conservation schemes are proposed. One is to use the meridional mass transport conservation equation as a constraint to derive the meridional wind first, and then the vertically integrated mass conservation equation is used to infer the zonal wind. The zonal and meridional winds are obtained separately in this approach. The second scheme is to use the vertically integrated mass conservation equation as a constraint to retrieve the zonal and meridional winds simultaneously from the first-guess field.

Temperature soundings from the Television and Infrared Observational Satellite (TIROS) Operational Vertical Sounder (TOVS) Pathfinder Path A dataset and a Special Sensor Microwave Imager (SSM/I) satellite-based surface wind field are used to derive the wind fields. The two mass conservation schemes yield two different wind fields. They are compared with the European Centre for Medium-Range Weather Forecasts (ECMWF) and National Centers for Environmental Prediction–National Center for Atmospheric Research (NCEP–NCAR) reanalyses and radiosonde observations over the Southern Ocean. The general circulation structure of both wind fields is similar to the reanalysis winds. However, the annual-mean bias of the first method is small in both the zonal and meridional winds compared to radiosonde observations, while the zonal wind bias of the second method is as large as -4 m s^{-1} . The main reason for the difference is that the second method requires that the Lagrange multiplier be zero on the latitudinal boundaries. This forces the retrieved zonal wind to approach the first-guess zonal wind. In contrast, the first method does not require latitudinal boundary conditions, allowing a larger correction to the first-guess zonal wind.

1. Introduction

An understanding of atmospheric energy and moisture transport over high latitudes is important for understanding global climate change. These studies require atmospheric wind profiles with reasonable accuracy and sufficient spatial and temporal resolutions to yield reliable flux estimates and to resolve their temporal variation. Atmospheric winds observed from aircraft and the radiosonde network, or derived from the satellite cloud-motion, do not have the spatial and temporal resolutions for accurate flux estimates. In particular, radiosonde stations are sparse over the oceans, aircraft observations are collected on an intermittent basis along fixed flight tracks and heights, and satellite cloud-drift winds only contain high- and low-level winds (e.g., Schmetz et al. 1993). For this reason, many recent en-

ergy and moisture flux studies are based on the wind fields from various analyses and reanalyses (e.g., Bromwich et al. 1995; Cullather et al. 1996, 2000; Wang and Paegle 1996; Genthon and Krinner 1998; Groves 2001). The most frequently used products are the European Centre for Medium-Range Weather Forecasts (ECMWF) analysis and reanalysis, National Centers for Environmental Prediction–National Center for Atmospheric Research (NCEP–NCAR) reanalysis, and National Meteorological Center (NMC) analysis. These winds have the advantages that they include various routine observations from satellites, ships, buoys, aircraft, and the radiosonde network, etc., combined with analysis/forecast models, which also contain a comprehensive set of physical parameterizations. They are easy to use because they are in gridded formats with global coverage for extended periods of time. Unfortunately, the analyses can contain spurious climate change signals resulting from frequent changes in the analysis models. To ameliorate these effects, reanalysis products were generated using frozen, state-of-the-art analysis/forecast

Corresponding author address: Dr. Cheng-Zhi Zou, Office of Research and Applications, NOAA/NESDIS, NOAA Science Center, Room 711, 5200 Auth Road, Camp Springs, MD 20746.
E-mail: cheng-zhi.zou@noaa.gov

models (Kalnay et al. 1996; Gibson et al. 1997). These reanalysis products, because of their duration, are often used as proxies for climate change studies.

Despite the obvious benefits, studies indicate that the wind fields in these reanalyses have large uncertainties, often producing different, and sometimes even conflicting, climatologies of the heat and moisture fluxes. For instance, Wang and Paegle (1996) showed that the wind differences, measured by a nondimensional root-mean-square ratio, between the NMC and ECMWF analyses are 2 to 3 times larger than their moisture differences. This large wind difference is the main cause of the large uncertainties in their moisture flux estimates over North America and South America. Cullather et al. (1996) show a close relationship between the El Niño–Southern Oscillation (ENSO) and the Antarctic moisture flux convergence calculated using the ECMWF operational analyses as well as the NCEP–NCAR reanalyses. In contrast, Genthon and Krinner (1998) found no convincing correlation between ENSO and the ECMWF reanalysis data. Bromwich et al. (2000) show that the different climate variability of the moisture flux convergence between the ECMWF analyses and reanalyses is caused by the differences in their wind fields.

The wind differences in the various analyses can be attributed to many causes. For instance, differences noted by Wang and Paegle (1996) in the NMC and ECMWF analysis winds were attributed to different physical parameterizations used to simulate low-level jets associated with topography. On the other hand, wind field differences between the ECMWF analysis and reanalysis in Bromwich et al. (2000) can be attributed to a height error in the reanalysis assimilation of the Vostok station on the Antarctic continent. Furthermore, because of the complicated error structure resulting from assimilation of various types of observations and different model parameterization schemes, it is often difficult to identify the specific causes of the errors in the analysis/reanalysis winds. Indeed, Francis and Cermak (2001) find that the ECMWF and NCEP–NCAR reanalyses winds exhibit systematic biases of up to 3 to 4 m s^{−1} in the middle and upper troposphere of the Arctic region when compared to independent radiosonde observations. The reasons for these errors are not yet clear.

The above difficulties in using the analysis/reanalysis winds call for improved reanalyses. The NCEP–NCAR Reanalysis II dataset has corrected some of the known problems in the NCEP–NCAR reanalysis (Kistler et al. 2001), and may provide improved understanding of the heat and moisture flux climatology in high latitudes. On the other hand, different wind products such as the purely satellite-based geostrophic wind may be used to provide a basic constraint on, and improved understanding of, the high-latitude wind climatology. For this reason, Slonaker and Van Woert (1999) and Zou and Van Woert (2001) attempted to derive a satellite-based, geostrophic-like wind dataset for the moisture flux and net pre-

cipitation estimates over the Southern Ocean. In Slonaker and Van Woert (1999), atmospheric meridional wind profiles were derived from the satellite-based surface wind field and the satellite temperature soundings based on the thermal wind relationship. Zou and Van Woert (2001, hereafter ZVW01) extended their wind derivation algorithm by including the mass conservation in a variational procedure. The retrieved annual-mean meridional wind in ZVW01 agrees with the radiosonde observations (raob) at the Macquarie Island, Tasmania station to within ± 0.5 m s^{−1} and its general circulation structure is also compatible with the ECMWF and NCEP–NCAR reanalyses. Compared to reanalysis systems that use primitive equation models, diverse observations, and complicated physical parameterizations, the satellite-retrieved winds have a much simpler error structure. Furthermore, satellite-derived winds are capable of reproducing the basic structure of the atmosphere with reasonable accuracy, and thus provides an attractive alternative for wind-related climate studies over the middle- and high-latitude oceans.

In ZVW01, only meridional wind profiles were derived. In this study, the wind derivation approach of the thermal wind plus mass conservation constraint developed in ZVW01 is applied to derive both zonal and meridional winds. Two forms of mass conservation constraints are presented and examined. The resultant atmospheric general circulation structure is then compared with the ECMWF and NCEP–NCAR reanalyses. To assess the performance of the algorithm, the resultant wind profiles are also compared to the raob at Macquarie Island. Through comparisons with the reanalyses and radiosonde measurements, this study attempts to provide a foundation for further application of these retrieval algorithms and the resultant wind profiles to climate diagnostic studies.

The next section describes the data used in this study. Section 3 describes the algorithms used to infer the wind field. Section 4 provides comparisons of the satellite-derived winds with the ECMWF and NCEP–NCAR reanalyses. Section 5 discusses the differences between the two mass conservation methods and section 6 provides comparisons between the satellite winds and radiosonde winds at Macquarie Island. Section 7 contains a summary.

2. Data

The satellite data used in this study are the same as in ZVW01. The surface wind field is the Special Sensor Microwave Imager–based (SSM/I) variational analysis wind obtained by Atlas et al. (1996). This surface wind is available globally every 6 h since July 1987 with a spatial resolution of 2° latitude by 2.5° longitude. This dataset uses the ECMWF 10-m analysis wind as the background and optimally blends nearly all available surface wind data, including conventional ship and buoy wind vectors, SSM/I wind speeds, and most of the Trop-

ical Atmospheric Ocean (TAO) array of moored buoys into the background field. Over the ocean area, wind velocities are significantly influenced by the SSM/I wind speeds. The SSM/I wind speeds have an accuracy of $\pm 2 \text{ m s}^{-1}$ with better coverage and resolution than in situ measurements. Therefore, the speed and direction of the blended surface wind vectors, referred to as VAM winds, exhibit higher accuracy than the original ECMWF 10-m wind when compared against independent buoy data. This is especially true over the tropical and Northern Hemispheric oceans (Atlas et al. 1996). Near Antarctica and the Southern Ocean, the VAM winds tend to present a better-defined circulation and more smoothly varying features when compared against the Comprehensive Ocean–Atmosphere Dataset (CO-DAS). Only the Southern Ocean portion of the dataset is used in this study.

The temperature data were taken from the Television and Infrared Observational Satellite (TIROS) Operational Vertical Sounder (TOVS) Pathfinder Path A dataset. Susskind et al. (1997) described the detailed characteristics of this dataset. TOVS Path A data are based on the interactive physical retrieval schemes of the Goddard Laboratory for Atmosphere (GLA). In this interactive retrieval system, the retrieval subsystem depends on the first-guess field, which is provided by the 6-h forecast of the GLA general circulation model; the retrieved satellite soundings, as well as other in situ concurrent measurements, are in turn used as the initial field for the next 6-h forecast. Susskind and Pfaendtner (1989) showed a significant positive improvement in skill of forecasts (and thus the first-guess for retrievals) using this interactive forecast–retrieval–assimilation system compared to those using operationally produced satellite soundings. The retrieved TOVS Path A temperature at 500 hPa has a global bias of 0.13 K and standard deviation of 1.40 K when validated against radiosonde observations (Susskind et al. 1997).

Daily mean temperature retrievals of TOVS Path A are available globally on a 1° latitude by 1° longitude grid. The dataset contains temperature outputs at the standard pressure levels and auxiliary layer-mean virtual temperature (Susskind et al. 1997). In this study we use the layer-mean virtual temperature defined at the layers of 1000–850, 850–700, 700–500, 500–300, and 300–100 hPa. Horizontal temperature gradients, and hence the thermal wind, are calculated from these temperature data. TOVS retrievals are performed only under clear or partially cloudy (up to 80% sky cover) conditions (Susskind 1993), resulting in data-void areas for totally overcast conditions. Within individual missing data areas, the temperature gradients in the longitudinal or latitudinal direction are approximated by the gradient obtained from the two surrounding good data in that direction. ZVW01 indicated that this approximation for the unresolved overcast areas would not significantly

affect the annual-mean winds, but would most likely underestimate the eddy winds.

The TOVS Pathfinder Path A daily data have been interpolated by Slonaker and Van Woert (1999) onto a 2° latitude by 2.5° longitude grid with a 6-h interval to match the VAM surface wind data. Only data for 1988 are used in this study.

3. Derivation of satellite wind

Over the middle and high latitudes, the thermal wind equations are good approximations to the momentum equations. The thermal wind equations and the continuity equation for an atmosphere in hydrostatic balance in spherical and isobaric coordinates are written as

$$\frac{\partial u_g}{\partial \ln p} = \frac{R_d}{f} \frac{\partial T^v}{a \partial \varphi} \quad (1)$$

$$\frac{\partial v_g}{\partial \ln p} = -\frac{R_d}{f} \frac{\partial T^v}{a \cos \varphi \partial \theta} \quad (2)$$

$$\frac{\partial u}{a \cos \varphi \partial \theta} + \frac{\partial (v \cos \varphi)}{a \cos \varphi \partial \varphi} + \frac{\partial \omega}{\partial p} = 0, \quad (3)$$

where a is the earth's radius, f the Coriolis parameter, R_d the dry air gas constant, T^v the virtual temperature, θ the longitude, φ the latitude, p the pressure; u , v , and ω are zonal, meridional and vertical p velocities, respectively; and u_g and v_g are the geostrophic zonal and meridional wind speeds, respectively. The top and bottom of our model atmosphere are assumed to be $p_T = 100 \text{ hPa}$ and $p_0 = 1000 \text{ hPa}$, respectively, in accordance with the available virtual temperature data. The surface wind is also assigned to the 1000-hPa level. Because of the constant pressure assumptions at the upper and bottom boundaries, the boundary conditions for no mass transport through the boundaries are simply $\omega = 0$ at $p = p_T$ and $p = p_0$ (Kasahara 1974). With these boundary conditions, the vertical velocity in (3) can be eliminated through integration over p from the surface to the top of the model atmosphere. The resultant mass conservation equation in a vertical atmospheric column is

$$\int_{p_T}^{p_0} \left[\frac{\partial u}{a \cos \varphi \partial \theta} + \frac{\partial (v \cos \varphi)}{a \cos \varphi \partial \varphi} \right] dp = 0. \quad (4)$$

Note that in variable surface pressure conditions, the vertical integral of the divergence is related to the surface pressure tendency plus the surface pressure advection (Kasahara 1974; Haltiner and Williams 1980). The constant surface pressure assumption results in the approximate mass conservation equation (4). This approximation greatly simplifies the retrieval algorithms. However, constant surface pressure assumption also introduces errors into the retrieved wind. In particular,

over the Southern Ocean area that is the focus of this study, annual-mean surface pressure ranges from 980 to 1005 hPa (Fig. 1) with small seasonal variations (± 5 hPa) (Peixóto and Oort 1992). Therefore, the 1000-hPa surface pressure assumption results in a height assignment error of the surface wind of ~ 20 hPa under lower surface pressure conditions. Using Eqs. (1) and (2) and the typical middle- and high-latitude values of synoptic systems, $\Delta T = 10 \sim 15$ K, $\Delta L = 1000$ km, and $f = 1.2 \times 10^{-4} \text{ s}^{-1}$, produces surface wind shear estimates of $|\partial u/\partial p| = |\partial v/\partial p| = 0.02 \sim 0.04 \text{ m s}^{-1} \text{ hPa}^{-1}$. Therefore, a 20-hPa height error would translate into a wind speed error of $0.5 \sim 0.7 \text{ m s}^{-1}$. To eliminate this error, the surface wind can be converted to 1000-hPa wind by using some assumed surface wind profiles (e.g., Boutin and Etcheto 1996). Because this error does not influence our discussions on the atmospheric general circulation structure and comparisons with radiosonde observations at Macquarie Island (ZVW01), we did not perform such a conversion. However, over plateau and mountain regions, such as the Antarctic continent, surface pressure can reach as low as 600-hPa (Fig. 1). In these regions, large surface wind errors could occur as a result of the constant surface pressure assumption.

In this study's satellite wind derivation, it is convenient to express (4) in a vertical differencing form. Using the trapezoidal rule and assuming $N + 1$ vertical atmospheric levels, after manipulating the vertical indexes, (4) can be written as

$$\sum_{k=0}^N f_k \left(\frac{\partial u_k}{a \cos \varphi \partial \theta} + \frac{\partial (v \cos \varphi)_k}{a \cos \varphi \partial \varphi} \right) = 0, \quad (5)$$

where

$$f_k = \begin{cases} 0.5\Delta p_0, & k = 0 \\ 0.5(\Delta p_k + \Delta p_{k-1}), & k = 1, 2, \dots, N-1 \\ 0.5\Delta p_{N-1}, & k = N \end{cases} \quad (6)$$

k is the vertical level index, and $\Delta p_k = p_k - p_{k+1}$ is the pressure difference between the two adjacent levels k and $k + 1$.

We follow the approach of Slonaker and Van Woert (1999) and ZVW01, in which the VAM or observed surface winds are used for the lower boundary in the satellite wind derivation. Integrating (1) and (2) with respect to p from the surface p_0 to any level p_k , the resultant integral equations are

$$\tilde{u}_k = u_0 - \sum_{n=1}^k \frac{R_d}{f} \frac{\partial T_{n-1/2}^v}{a \partial \varphi} \ln \frac{p_{n-1}}{p_n}, \quad k = 1, 2, \dots, N, \quad \text{and} \quad (7)$$

$$\tilde{v}_k = v_0 + \sum_{n=1}^k \frac{R_d}{f} \frac{\partial T_{n-1/2}^v}{a \cos \varphi \partial \theta} \ln \frac{p_{n-1}}{p_n}, \quad k = 1, 2, \dots, N, \quad (8)$$

where u_0 and v_0 are the observed surface winds, $T_{n-1/2}^v$ is the layer mean virtual temperature between the levels $n - 1$ and n , and \tilde{u} and \tilde{v} are the Slonaker and Van Woert (1999) type of pseudogeostrophic winds. They are pseudogeostrophic because u_0 and v_0 include ageostrophic components.

ZVW01 showed that this type of pseudogeostrophic wind was nonmass-conserved. This feature can be illustrated by introducing (7) and (8) into (5). Noticing that the derivatives of the thermal wind parts in \tilde{u} and \tilde{v} cancel out, the divergence in a whole vertical column of the atmosphere generated by \tilde{u} and \tilde{v} reduces to the surface divergence multiplied by the thickness of the whole atmosphere, that is,

$$\begin{aligned} & \sum_{k=0}^N f_k \left(\frac{\partial \tilde{u}_k}{a \cos \varphi \partial \theta} + \frac{\partial (\tilde{v} \cos \varphi)_k}{a \cos \varphi \partial \varphi} \right) \\ &= (p_0 - p_N) \left[\frac{\partial u_0}{a \cos \varphi \partial \theta} + \frac{\partial (v_0 \cos \varphi)}{a \cos \varphi \partial \varphi} \right]. \end{aligned} \quad (9)$$

Because u_0 and v_0 include ageostrophic components, their divergence is nonzero for both cyclone- and global-scale atmospheric motions. In the following, two different methods are presented to force the divergence to be zero and hence conserve mass.

a. Deriving zonal and meridional winds separately

In this method, an extension of the ZVW01 approach is used to derive the mass-conserved zonal and meridional winds separately. Integrating (5) over a zonal circle and over latitude from a pole to a latitude φ , and given that $\cos \varphi$ is zero at the poles, one obtains the following equation for the total net mass transport through a latitudinal wall,

$$\int_0^{2\pi} \sum_{k=0}^N f_k v_k a \cos \varphi d\theta = 0. \quad (10)$$

Based on surface pressure observations, Oort and Peixóto (1983) suggested that the zonal and vertical mean meridional velocities should be on the order of 1 mm s^{-1} on a seasonal timescale. Therefore, Eq. (10) is a good approximation for the meridional mass transport conservation, and thus becomes a requirement for the meridional wind to satisfy (Oort and Peixóto 1983). In ZVW01, the variational formalism for obtaining the mass-conserved meridional wind, v , is to minimize the differences between v and \tilde{v} in a least-squares sense subject to the mass transport constraint Eq. (10), that is,

$$\begin{aligned} E = & \int_0^{2\pi} \sum_{k=1}^N \alpha_k (v_k - \tilde{v}_k)^2 a \cos \varphi d\theta \\ & + \lambda \int_0^{2\pi} \sum_{k=0}^N f_k v_k a \cos \varphi d\theta, \end{aligned} \quad (11)$$

where λ is a Lagrange multiplier and α_k is an a priori specified weighting function. Equation (11) is expressed on a latitudinal wall, so E and λ have different values at different latitudes. The weighting function α_k can be specified arbitrarily (Daley 1991). ZVW01 indicated that a vertically uniform weighting function resulted in a meridional wind structure comparable to the radiosonde observations at Macquarie Island. Therefore, the weighting function is assumed to be 1 throughout this study. The solution for v_k from (11) is given by (ZVW01),

$$v_k = \tilde{v}_k - \frac{1}{2}f_k\lambda, \quad k = 1, \dots, N, \quad (12)$$

where λ is obtained by introducing (12) into (10), giving

$$\lambda = \frac{\int_0^{2\pi} d\theta \sum_{k=0}^N f_k \tilde{v}_k}{2\pi \sum_{k=1}^N \frac{1}{2}f_k f_k}. \quad (13)$$

Here we have used $v_0 = \tilde{v}_0$ because the observed surface wind is specified during the wind derivations.

Equations (8), (12), and (13) provide a complete solution for the mass-conserved meridional wind (ZVW01). Assuming the meridional wind is now known, the zonal wind, u , can be obtained similarly by a variational formalism in which the differences between u and \tilde{u} are minimized in a least-squares sense subject to the mass conservation constraint (5). The variational formalism at any latitude, φ , using Eq. (5) as a strong constraint is written as

$$E = \int_0^{2\pi} \sum_{k=1}^N (u_k - \tilde{u}_k)^2 a \cos \varphi d\theta + \int_0^{2\pi} \lambda_1 \sum_{k=0}^N f_k \left[\frac{\partial u_k}{a \cos \varphi \partial \theta} + \frac{\partial (v \cos \varphi)_k}{a \cos \varphi \partial \varphi} \right] a \cos \varphi d\theta. \quad (14)$$

In this situation, the Lagrange multiplier λ_1 is a function of longitude. Taking the first variation of (14), integrating by parts, and considering v and u_0 as specified, we obtain

$$\begin{aligned} \delta E = & \int_0^{2\pi} \sum_{k=1}^N 2(u_k - \tilde{u}_k) \delta u_k a \cos \varphi d\theta + \sum_{k=1}^N f_k [\delta u_k \lambda_1] \Big|_0^{2\pi} \\ & - \int_0^{2\pi} \sum_{k=1}^N f_k \delta u_k \frac{\partial \lambda_1}{\partial \theta} d\theta \\ & + \int_0^{2\pi} \delta \lambda_1 \sum_{k=0}^N f_k \left[\frac{\partial u_k}{a \cos \varphi \partial \theta} + \frac{\partial (v \cos \varphi)_k}{a \cos \varphi \partial \varphi} \right] a \cos \varphi d\theta \end{aligned} \quad (15)$$

To obtain an optimal solution, the boundary terms should vanish and δE must be zero for any choice of δu_k and $\delta \lambda_1$. At the longitudinal boundaries, we have

periodic conditions for the zonal wind, that is, $u(0) = u(2\pi)$. Therefore, there are three choices that allow the boundary term, $[\delta u_k \lambda_1] \Big|_0^{2\pi}$, to be zero. One is to specify the wind values at the boundaries. However, this is unrealistic. Hence, either periodic boundary conditions or zero boundary conditions (which is called the natural boundary condition, see e.g., Daley 1991) for λ_1 are required. In this study, we have chosen to use the periodic boundary conditions. However, as will be shown later, the zero boundary conditions would lead to the same results.

With the given boundary conditions, the Euler-Lagrange equation of (15) leads to a pair of equations. One is the constraint equation (5), and the other is the following solution for u_k ,

$$u_k = \tilde{u}_k + \frac{1}{2}f_k \frac{\partial \lambda_1}{a \cos \varphi \partial \theta}, \quad k = 1, 2, \dots, N. \quad (16)$$

Substituting (16) into (5), one obtains a second-order ordinary differential equation for λ_1 ,

$$\frac{\partial^2 \lambda_1}{\partial \theta^2} = -a^2 \cos^2 \varphi \frac{\sum_{k=0}^N f_k \left[\frac{\partial \tilde{u}_k}{a \cos \varphi \partial \theta} + \frac{\partial (v \cos \varphi)_k}{a \cos \varphi \partial \varphi} \right]}{\sum_{k=1}^N \frac{1}{2}f_k f_k}. \quad (17)$$

Because both \tilde{u} and v are already known, the right-hand side of (17), denoted as $H(\theta, \varphi)$, is known. Direct integration of (17) gives the solution for λ_1 ,

$$\lambda_1 = \int_{\theta_0}^{\theta} G(\theta_0, \gamma, \varphi) d\gamma + C_0 \theta + C_1, \quad (18)$$

where C_0 and C_1 are as yet undetermined constants, γ is an integration variable, $G(\theta_0, \theta, \varphi) \equiv \int_{\theta_0}^{\theta} H(\gamma, \varphi) d\gamma$, and θ_0 is an initial point for integration. Utilizing the periodic boundary condition $\lambda_1(\theta_0) = \lambda_1(\theta_0 + 2\pi)$, C_0 can be determined as

$$C_0 = -\frac{1}{2\pi} \int_{\theta_0}^{\theta_0+2\pi} G(\theta_0, \gamma, \varphi) d\gamma = -\overline{G}(\theta_0, \varphi), \quad (19)$$

where $\overline{G}(\theta_0, \varphi)$ is the zonally averaged $G(\theta_0, \theta, \varphi)$. Notice that for zero boundary conditions of λ_1 , C_0 would be exactly the same as Eq. (19).

Using (19), the first-order derivative of (18) becomes

$$\frac{\partial \lambda_1}{\partial \theta} = G(\theta_0, \theta, \varphi) - \overline{G}(\theta_0, \varphi). \quad (20)$$

Because only $\partial \lambda_1 / \partial \theta$ is needed in the zonal wind solution (16), the unknown constant C_1 does not need to be determined.

Note that (20) provides a unique solution for $\partial \lambda_1 / \partial \theta$ that does not depend on the selection of θ_0 . In particular, assuming there is another initial point θ'_0 , it is easily demonstrated that

$$\begin{aligned} G(\theta_0, \theta, \varphi) - \overline{G}(\theta_0, \varphi) \\ = G(\theta'_0, \theta, \varphi) - \overline{G}(\theta'_0, \varphi). \end{aligned} \quad (21)$$

Therefore, in the actual calculations, we simply choose $\theta_0 = 0$. In addition, a smoothing process has been applied to the term $\partial\lambda_1/\partial\theta$. Equation (17) shows that this term is related to the divergence term $\partial\tilde{u}_k/\partial\theta + \partial(v \cos\varphi)_k/\partial\varphi$. Noise associated with gravity waves or the differencing approximation may emerge from the calculation of this term. In our calculation, a low-pass filter with a cutoff distance equal to the Rossby radius of deformation has been applied in the latitudinal direction to filter out noise in $\partial\lambda_1/\partial\theta$. In addition, a cosine-type filter was applied to the remaining wavenumbers in order to provide a smooth transition near the cutoff wave.

The previous procedure gives a complete solution for the mass-conserved meridional and zonal winds provided the temperature soundings and surface wind fields are known.

b. Deriving zonal and meridional winds simultaneously

The mass-conserved zonal and meridional winds can also be obtained simultaneously by adjusting both components in the variational functional. In this situation, the variational formalism using (5) as a strong constraint is written as

$$\begin{aligned} E = \int_0^{2\pi} \int_{\varphi_1}^{\varphi_2} \sum_{k=1}^N [(u_k - \tilde{u}_k)^2 + (v_k - \tilde{v}_k)^2] a^2 \cos\varphi \, d\theta \, d\varphi \\ + \int_0^{2\pi} \int_{\varphi_1}^{\varphi_2} \lambda_2 \sum_{k=0}^N f_k \left[\frac{\partial u_k}{a \cos\varphi \partial\theta} + \frac{\partial(v \cos\varphi)_k}{a \cos\varphi \partial\varphi} \right] a^2 \cos\varphi \, d\theta \, d\varphi, \end{aligned} \quad (22)$$

where φ_1 and φ_2 are latitudinal boundaries within which the winds are obtained. This type of variational formalism is often used in the data initialization for removing external gravity waves (e.g., Sasaki et al. 1979; Haltiner and Williams 1980) and also used in the polynomial smoothing processes on the radiosonde winds (Gruber and O'Brien 1968). Unlike Eqs. (11) and (14), which are for a latitudinal wall, Eq. (22) is

for a whole latitude band bounded by φ_1 and φ_2 and the Lagrange multiplier λ_2 is a function of both latitude and longitude. Thus, it requires boundary conditions in both directions. Again, taking the first variation of (22), integrating by parts, and considering v_0 and u_0 as being specified, one obtains a variation equation analogous to (15) but with both the zonal and meridional winds included, that is,

$$\begin{aligned} \delta E = \int_0^{2\pi} \int_{\varphi_1}^{\varphi_2} \sum_{k=1}^N [2(u_k - \tilde{u}_k)\delta u_k + 2(v_k - \tilde{v}_k)\delta v_k] a^2 \cos\varphi \, d\theta \, d\varphi + \int_{\varphi_1}^{\varphi_2} \sum_{k=1}^N f_k [\delta u_k \lambda_2]_{\varphi_1}^{2\pi} a \, d\varphi \\ + \int_0^{2\pi} \sum_{k=1}^N f_k [\delta v_k \lambda_2 \cos\varphi]_{\varphi_1}^{\varphi_2} a \, d\theta - \int_0^{2\pi} \int_{\varphi_1}^{\varphi_2} \sum_{k=1}^N f_k \left(\delta u_k \frac{\partial \lambda_2}{a \cos\varphi \partial\theta} + \delta v_k \frac{\partial \lambda_2}{a \partial\varphi} \right) a^2 \cos\varphi \, d\theta \, d\varphi \\ + \int_0^{2\pi} \int_{\varphi_1}^{\varphi_2} \delta \lambda_2 \sum_{k=0}^N f_k \left[\frac{\partial u_k}{a \cos\varphi \partial\theta} + \frac{\partial(v \cos\varphi)_k}{a \cos\varphi \partial\varphi} \right] a^2 \cos\varphi \, d\theta \, d\varphi. \end{aligned} \quad (23)$$

For the zonal direction, periodic boundary conditions similar to the ones chosen for λ_1 are used for λ_2 . At the latitudinal boundaries, because v can neither be specified nor is it periodic, the natural condition $\lambda_2|_{\varphi_1} = \lambda_2|_{\varphi_2} = 0$ is used to ensure that the term $[\delta v_k \lambda_2 \cos\varphi]_{\varphi_1}^{\varphi_2}$ vanishes.

The Euler–Lagrange equations of (23) give the following solution for the mass-conserved zonal and meridional winds,

$$u_k = \tilde{u}_k + \frac{1}{2} f_k \frac{\partial \lambda_2}{a \cos\varphi \partial\theta}, \quad k = 1, 2, \dots, N, \quad (24)$$

and

$$v_k = \tilde{v}_k + \frac{1}{2} f_k \frac{\partial \lambda_2}{a \partial\varphi}, \quad k = 1, 2, \dots, N. \quad (25)$$

Introducing (24) and (25) into (5), one obtains a Poisson equation for λ_2 ,

$$\begin{aligned} & \frac{\partial^2 \lambda_2}{a^2 \cos^2 \varphi \partial \theta^2} + \frac{\partial}{a^2 \cos \varphi \partial \varphi} \left(\cos \varphi \frac{\partial \lambda_2}{\partial \varphi} \right) \\ &= - \frac{\sum_{k=0}^N f_k \left[\frac{\partial \tilde{u}_k}{a \cos \varphi \partial \theta} + \frac{\partial (\tilde{v} \cos \varphi)_k}{a \cos \varphi \partial \varphi} \right]}{\sum_{k=1}^N \frac{1}{2} f_k f_k}. \end{aligned} \quad (26)$$

Because wind data are provided at grid points, it is more convenient to write (26) in finite centered-difference form in the longitudinal direction, that is,

$$\begin{aligned} & \frac{1}{a^2 \cos^2 \varphi (\Delta \theta)^2} (\lambda_{2i+1/2} - 2\lambda_{2i-1/2} + \lambda_{2i-3/2}) \\ & + \frac{\partial}{a^2 \cos \varphi \partial \varphi} \left(\cos \varphi \frac{\partial \lambda_{2i-1/2}}{\partial \varphi} \right) = C_{i-1/2} \\ & i = 1, 2, \dots, M, \end{aligned} \quad (27)$$

where i is the longitude index and C represents the right-hand side of (26). The longitudinal boundary condition becomes $\lambda_{2-1/2} = \lambda_{2M+1/2}$. The discrete Fourier expansions that satisfy the periodic condition are

$$\begin{aligned} \lambda_{2i-1/2} &= \frac{1}{M} \sum_{m=0}^{M-1} \Lambda_m e^{-2\pi j i m / M}, \\ C_{i-1/2} &= \frac{1}{M} \sum_{m=0}^{M-1} \chi_m e^{-2\pi j i m / M}, \end{aligned} \quad (28)$$

where $j = \sqrt{-1}$, and Λ_m and χ_m are the Fourier expansion coefficients of λ_2 and C , respectively. Introducing (28) into (27), one obtains

$$\begin{aligned} & \frac{2 \left(\cos \frac{2\pi m}{M} - 1 \right)}{a^2 \cos^2 \varphi (\Delta \theta)^2} \Lambda_m + \frac{\partial}{a^2 \cos \varphi \partial \varphi} \left(\cos \varphi \frac{\partial \Lambda_m}{\partial \varphi} \right) \\ &= \chi_m, \quad m = 0, 1, \dots, M-1. \end{aligned} \quad (29)$$

Equation (29) is a set of second-order ordinary differential equations with the boundary conditions $\Lambda_m|_{\varphi_1} = \Lambda_m|_{\varphi_2} = 0$, $m = 0, 1, \dots, M-1$. This is solved in this study using an extension of the Gaussian elimination method described in Lindzen and Kuo (1969).

In the actual calculation, the fast Fourier transform is first performed on C to obtain χ_m at each latitude and then Eq. (29) is solved for Λ_m . After Λ_m is obtained, an inverse fast Fourier transform is used to obtain the solution for λ_2 at each grid point. The mass-conserved winds can be then obtained from (24) and (25).

Using the satellite layer-mean virtual temperature profiles and surface wind observations, the mass-conserved and nonmass-conserved winds are obtained at the levels of 850, 700, 500, 300, and 100 hPa. The retrieval region extends from 50° to 76°S, but this study analyzes only the Southern Ocean region from 50° to 65°S. There, the surface pressure is closer to the 1000 hPa, as discussed before. For convenience, u_{c1} and v_{c1} are used to refer

to the zonal and meridional winds obtained by the first mass conservation constraints and u_{c2} and v_{c2} to the second mass conservation constraint.

4. Monthly mean zonal-mean winds

For climate studies, the satellite-derived winds need to provide a reasonable representation of the atmospheric general circulation structure and also provide reasonable accuracy compared to radiosonde observations. In spite of the limitations inherent in the ECMWF and NCEP–NCAR reanalysis winds for climate variability studies, as discussed earlier, their basic atmospheric general circulation structure over short time periods can still provide a useful reference for satellite wind comparisons. Figures 2a–d and Figs. 3a–d show the satellite-derived, monthly averaged, Southern Ocean zonal-mean zonal wind, compared with the ECMWF and NCEP–NCAR reanalyses for January and July 1988, respectively. In the figures, both the ECMWF and NCEP–NCAR reanalysis plots use only the six vertical levels that correspond to the satellite data levels for a parallel comparison. The ECMWF and NCEP–NCAR reanalyses show almost identical zonal-mean zonal winds for the 2 months. Note that the mass conservation correction to the nonmass-conserved wind \tilde{u} depends on the longitudinal derivatives of the Lagrange multipliers in both (16) and (24). Because the zonal integrals of the correction terms are zero after using the periodic boundary conditions, the zonal-means of u_{c1} and u_{c2} are both equal to the zonal-mean of \tilde{u} . Therefore, Fig. 2a and Fig. 3a represent the satellite-derived zonal-mean zonal winds for both mass-conserved and nonmass-conserved formations.

The main feature in the zonal-mean zonal wind for the 2 months selected is the seasonal march of the jet stream positions associated with the seasonal variation of the atmospheric thermal structure. A complete analysis of the Southern Hemispheric ECMWF and NCEP–NCAR reanalysis data (not shown) indicates that the Southern Hemispheric jet stream was located near 45°S with an amplitude of approximately 30 m s⁻¹ during January 1988. The jet stream moved from about 45°S in January to about 30°S in July. Figures 2 and 3 show that the satellite-derived zonal wind basically captures the strength and position of the jet stream. In January, an almost-closed jet stream is observed near 300 hPa equatorward of 50°S with a strength of about 30 m s⁻¹. This is similar to the jet stream position observed in the ECMWF and NCEP–NCAR reanalyses. Note that because there is no 200-hPa level in the plots, the jet stream position that generally appears near 200 hPa in January (e.g., Van Loon 1972) now appears at 300 hPa. During July, the satellite-derived zonal wind shows much weaker horizontal shear near 50°S, indicating that it is far removed from the jet stream position. This is also similar to the reanalysis data.

Figures 2d and 3d show the difference fields between

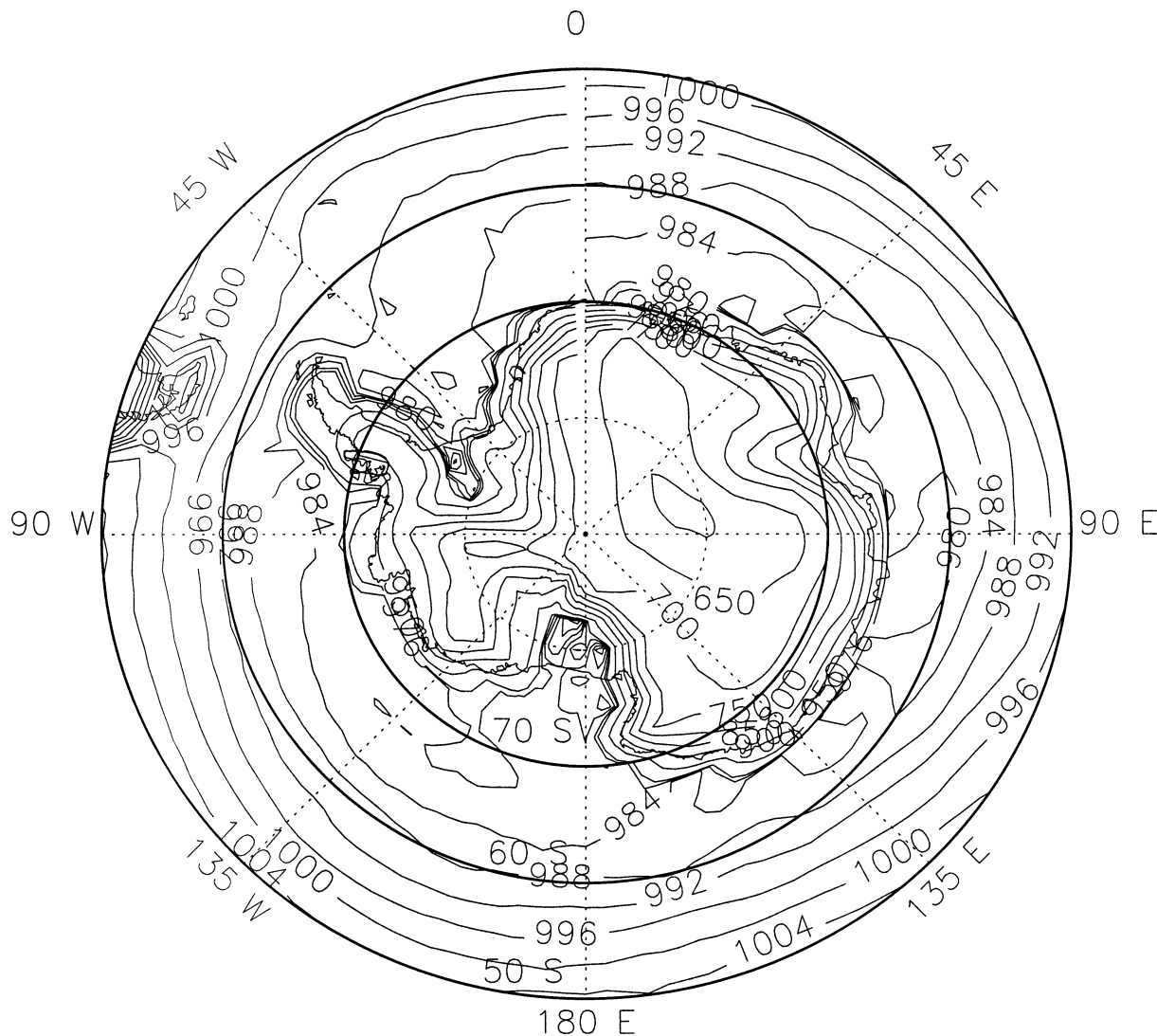


FIG. 1. 1988 annual-mean surface pressure from the ECMWF analysis over the Southern Ocean and Antarctica. Contour intervals are 4 hPa from 1004 to 980 hPa, 10 hPa from 980 to 950 hPa, and 50 hPa below 950 hPa.

the ECMWF reanalysis and the satellite-derived zonal-mean zonal wind. The differences between the satellite-derived and the NCEP–NCAR reanalyses are similar to these plots and, thus, are not shown here. The figures show that the differences are typically within 2.5 m s^{-1} throughout the troposphere for both months except near the tropopause. There the differences reach 5 m s^{-1} . These values are close to the differences between the ECMWF reanalysis and an ensemble mean from 31 atmospheric general circulation models in the Atmospheric Model Intercomparison Project (AMIP) (Gates et al. 1999) over the Southern Ocean (the ensemble has a bias of $2\text{--}2.5 \text{ m s}^{-1}$ compared to the ECMWF reanalysis and a standard deviation of $3\text{--}5 \text{ m s}^{-1}$ in the troposphere over the Southern Ocean). This indicates that the satellite algorithms yield a zonal-mean zonal wind struc-

ture similar to the reanalyses and most of the other general circulation models.

Figures 4a–g show the satellite-derived zonal-means of \bar{v} , v_{e1} , and v_{e2} compared with the ECMWF and NCEP–NCAR reanalyses for January 1988. The July 1988 plots (not shown) are similar to the January plots except for a slight poleward movement of the latitudinal boundary between the Ferrel cell and the polar cell. As can be seen from Eq. (8) and Fig. 4a, the zonal-mean \bar{v} is equal to the zonal-mean v_0 when there are no missing data because the integral of $\partial T^v/a \cos\phi \partial\theta$ over a zonal circle vanishes. This feature results in a zonal-mean structure of \bar{v} with a poleward flow throughout the troposphere equatorward of 63°S and an equatorward flow throughout the troposphere poleward of 63°S . Obviously, \bar{v} does not correctly represent the meridional

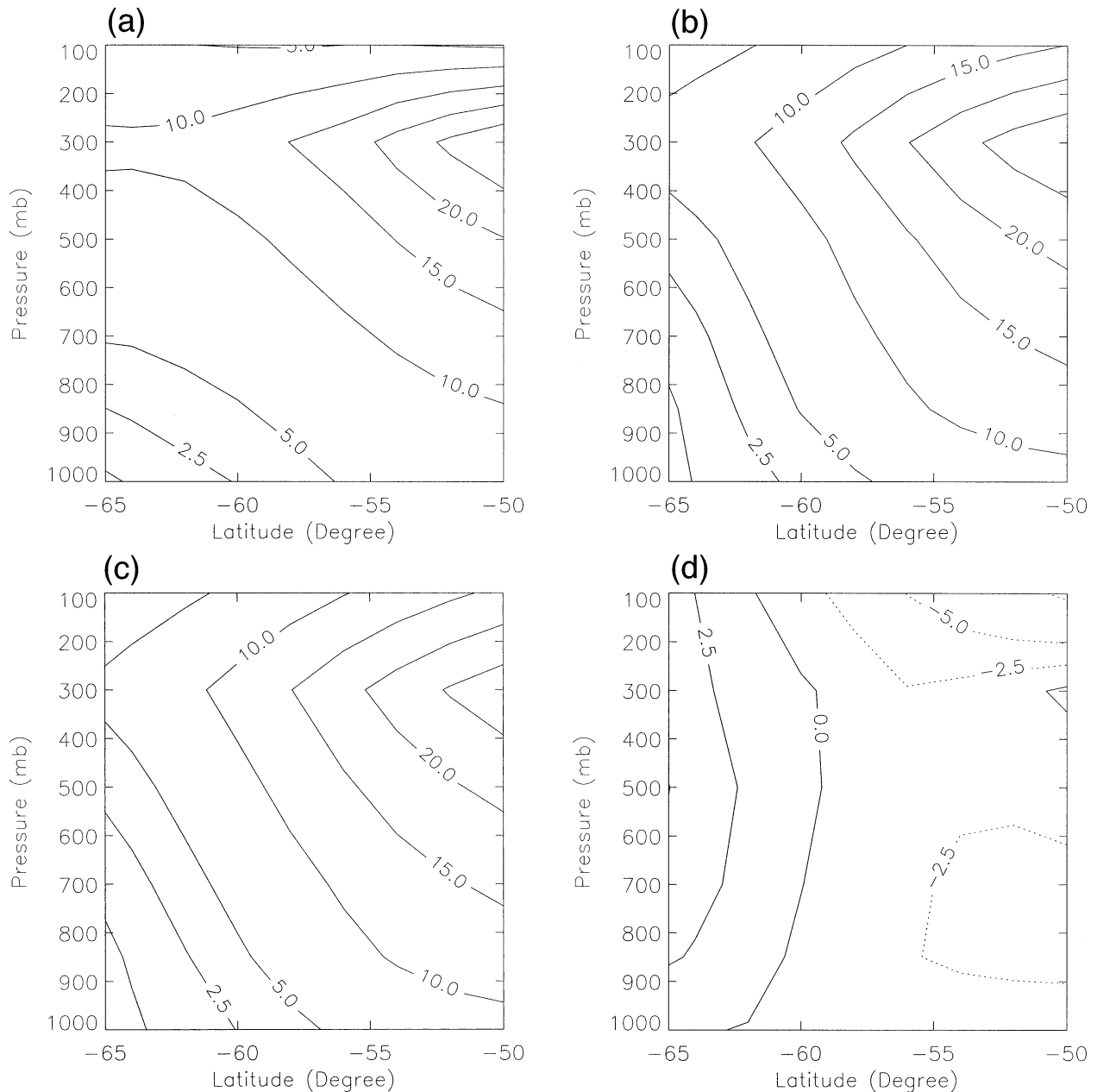


FIG. 2. Comparisons of the monthly and zonally averaged satellite and reanalysis zonal winds for Jan 1988. (a) u_{e1} ; (b) ECMWF reanalysis; (c) NCEP-NCAR reanalysis; (d) $u_{e1} - \text{ECMWF}$. Satellite data are smoothed using a five-point running mean. Contour intervals are 2.5 m s^{-1} for the wind values from -5 to 5 m s^{-1} and 5 m s^{-1} for the wind values larger than 5 m s^{-1} . Note that $u_{e1} = u_{e2} = \bar{u}$ for the zonal mean.

wind structure associated with the Ferrel cell and polar cell in the middle and high latitudes. This is the primary reason that the mass conservation correction was introduced by ZVW01.

Figures 4b and 4c show that the two mass conservation schemes for the satellite wind derivation yield similar structure and magnitudes for the zonal-mean meridional winds during the selected month. The zonal-mean differences between v_{e1} and v_{e2} are less than 0.2

m s^{-1} for January and 0.1 m s^{-1} for July over the ocean region. The basic structure of the satellite meridional winds is similar to the reanalysis winds except at the top level of the model atmosphere. There, both the ECMWF and NCEP-NCAR reanalyses show weak northward zonal-mean wind between 50° and 63°S while the satellite winds are southward. ZVW01 suggest that more observations are needed to resolve this difference. In the lower troposphere, the satellite-derived thickness

of the southerly wind regime near the planetary boundary layer (lower branch of the Ferrel cell) is intermediate to the ECMWF and NCEP–NCAR reanalyses. Also, the amplitudes of the satellite surface winds are intermediate to the ECMWF and NCEP–NCAR products, with peak values that are 25% weaker than the NCEP–NCAR data, but 50% stronger than the ECMWF data for both months. The amplitude differences between the satellite-derived and reanalysis winds can also be seen in the difference fields, Figs. 4f and 4g, where the differences reach 0.5 m s^{-1} near the ocean surface between 50° and 55°S .

It is of interest to compare the surface zonal wind differences between various products with the differences of the meridional components. Such a comparison for July 1988 is shown in Fig. 5. It is seen that the differences between the VAM, ECMWF, and NCEP–NCAR reanalyses surface winds are on the order of 0.5 to 1 m sec^{-1} for both the zonal and meridional components over the entire Southern Ocean. Since the magnitude of the zonal-mean meridional wind is small, these differences yield a larger relative error (50%–100%) in the meridional circulation among the various products. For the zonal component, however, the relative difference is smaller (10%–20%) when the surface wind is large (e.g., near 50°S) and larger when the surface wind is small (e.g., near 65°S). Part of these differences could reflect errors inherited in the satellite wind measurements. Specifically, the VAM wind has a bias on the order of 0.5 m sec^{-1} (Atlas et al. 1996). On the other hand, these differences could reflect errors in the model-simulated surface wind, since the satellite-observed surface wind was not assimilated into the ECMWF and NCEP–NCAR reanalyses. Within the framework of the middle- and high-latitude zonal-mean circulation theory, the zonal surface wind can be determined from the approximate balance between the zonal surface stress and the vertically integrated convergence of the eddy momentum flux (e.g., Green 1970). In contrast, the zonal-mean meridional circulation is determined by the imbalance between the convergence of the eddy heat and momentum transport and the atmospheric heating and friction (including the planetary boundary layer friction and cumulus friction) (Lorenz 1967; Schneider and Lindzen 1977; Held and Hou 1980). This imbalance requires a weak Ferrel cell to transport additional energy and momentum. The uncertainties in the parameterizations of some of those processes (e.g., the surface and cumulus friction) will influence the accuracy of the model-produced surface wind, especially for the zonal-mean meridional component. Indeed, errors of up to 50% to 100% exist in the zonal-mean meridional circulation among various models (e.g., Gates et al. 1999).

Despite the magnitude of the differences, all products show the same zonal-mean surface wind directions for both the zonal and meridional components over the Southern Ocean. Future assimilation of the satellite sur-

face winds in the reanalyses would most likely reduce the magnitude of these differences.

5. Longitudinal distribution

In the previous section, it was shown that the two mass conservation schemes give the same zonal means of u_{c1} and u_{c2} and similar zonal means of v_{c1} and v_{c2} . This section examines the impact of the different mass conservation schemes on the zonal distributions of the satellite winds. Again, the zonal structure of the satellite winds is first compared with reanalyses. Figures 6a–d and Figs. 7a–d show the zonal distributions of the monthly mean u_{c1} and u_{c2} compared with the ECMWF and NCEP–NCAR reanalyses at 54°S for January and July 1988. The zonal distribution of \bar{u} is not shown because it is almost identical to u_{c2} . Figures 6 and Fig. 7 show that both u_{c1} and u_{c2} exhibit structural variations during January and July that are similar to the ECMWF and NCEP–NCAR reanalysis data. In January, both satellite and reanalysis winds show a four-wave-like structure with four jet cores along the zonal direction near 300 hPa. The longitudinal locations of the jet cores are similar in the satellite and reanalysis winds. The satellite winds have slightly weaker ($\sim 5 \text{ m s}^{-1}$) jet amplitudes than the reanalysis data and weaker vertical shear in the lower troposphere. Near the tropopause, the satellite winds have steeper vertical shear than the reanalysis winds. In July, both satellite winds and reanalysis winds are characterized by a dominant wave number 1 structure with a strong wind regime over the Indian Ocean (around 60°E) and a weaker wind regime over the eastern South Pacific Ocean (around 100°W).

Figures 8a–e show the longitudinal distributions for January 1988 of the monthly mean \bar{v} , v_{c1} , and v_{c2} , as well as ECMWF and NCEP–NCAR reanalyses at 54°S . It is seen that the satellite winds, v_{c1} and v_{c2} , as well as the ECMWF and NCEP–NCAR reanalysis winds all show a three-wave-like pattern, similar to that described by Van Loon (1972). However, the nonmass-conserved wind \bar{v} fails to capture the equatorward flow over the Indian Ocean (60° – 100°E) and, as a result, fails to show the three-wave-like pattern. The longitudinal position of the poleward and equatorward jet centers in the satellite winds v_{c1} and v_{c2} compares quite well with the ECMWF and NCEP–NCAR reanalyses. However, the satellite wave amplitudes are generally weaker. A three-wave-like pattern also occurs in July (not shown), and the satellite-derived longitudinal positions of the poleward and equatorward jet centers are also similar to the reanalyses.

Though the two satellite winds have similar zonal structure and are also similar to the reanalysis winds, there are subtle differences between the satellite and reanalysis winds and between the satellite winds themselves. There are many reasons for the differences between the satellite and reanalysis winds. For instance, as mentioned before, the reanalyses have more sophis-

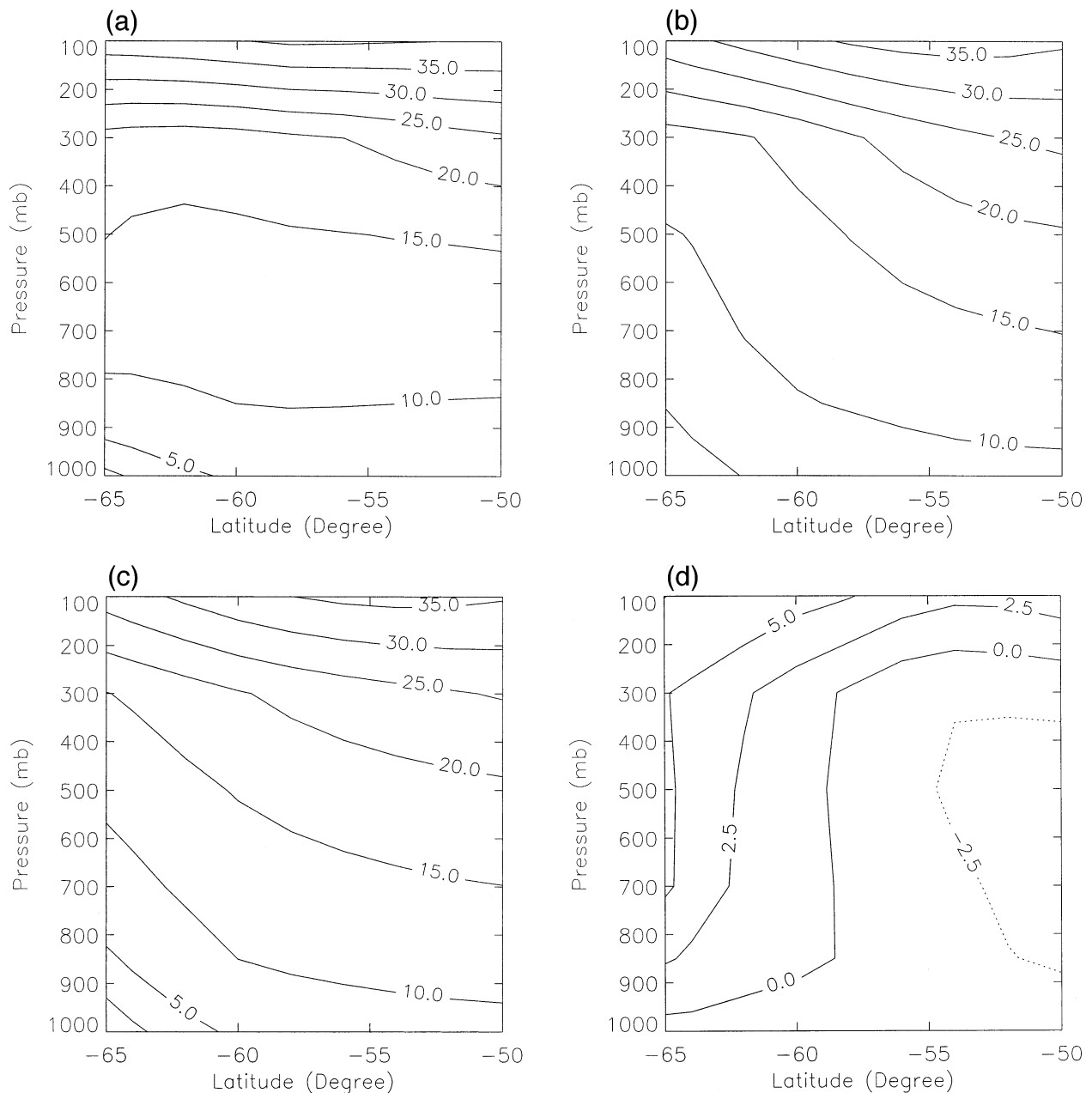


FIG. 3. Same as in Fig. 2 except for Jul 1988. (a) u_{c1} ; (b) ECMWF reanalysis; (c) NCEP-NCAR reanalysis; (d) $u_{c1} - \text{ECMWF}$. Contour intervals are 2.5 m s⁻¹ for the wind values from -5 to 5 m s⁻¹ and 5 m s⁻¹ for the wind values larger than 5 m s⁻¹.

licated dynamics and data assimilation schemes and include other types of observations. It is not the intent of this study to analyze these differences in detail. Rather, the focus is mainly on the differences between the two satellite wind products.

Figures 9a–b show the difference fields ($u_{c2} - u_{c1}$) for January and July 1988 at 54°S. These figures depict a phase shift between u_{c1} and u_{c2} characterized by a dominant wavenumber 1 oscillation plus a minor wavenumber 2 oscillation in the zonal direction. Fourier analysis at 500 hPa indicates that the wave 1 variance is

about 66% and 88% of the total variance in January and July, respectively; wave 2 variance is about 10% of the total variance in both months (wave variance is defined as the square of a wave amplitude and the total variance is the summation of all the wave's variance). The amplitudes of the oscillation are about 1–2 m s⁻¹ in January 1988 and reach 5–6 m s⁻¹ in July. Similar wave structure also occurs in the meridional wind difference field (v_{c2} minus v_{c1}) for January and July 1988 at 54°S as seen in Figs. 10a–b. Figure 10 shows that v_{c2} has a larger equatorward component than v_{c1} from 90°E to 180°

(eastern Indian Ocean to western South Pacific Ocean) in January 1988 and from 20° to 170°E (Indian Ocean to western South Pacific Ocean) in July.

To understand the different behavior of the two satellite winds, the maximum and average differences between any two wind fields a_1 and a_2 are utilized to quantify the differences. At any latitude φ , the maximum difference is the maximum absolute difference between a_1 and a_2 and the average difference D is defined as

$$D = \frac{1}{2\pi(p_0 - p_T)} \int_0^{2\pi} \int_0^{p_0} |a_1 - a_2| d\theta dp$$

$$= \frac{1}{2\pi(p_0 - p_T)} \int_0^{2\pi} \sum_{k=0}^N f_k |a_1 - a_2|_k d\theta. \quad (30)$$

Table 1 provides the maximum and average differences between various zonal wind products for January and July 1988 at 54°S. Table 2 is similar to Table 1 except it presents values for the meridional winds. As seen in Table 1, the maximum and average differences between \tilde{u} and u_{c2} are only around 0.7 m s⁻¹ and 0.2 m s⁻¹, respectively, for both months. These values are nearly an order of magnitude smaller than the differences between other variables, for example, \tilde{u} and u_{c1} , or \tilde{v} and v_{c2} . The reason for the small differences between \tilde{u} and u_{c2} can be attributed to the boundary conditions used for the Lagrange multiplier in the second mass conservation constraint. At the two latitudinal boundaries we have assumed $\lambda_2(\theta, \varphi_i) = 0$, where $i = 1$ or 2 . These boundary conditions lead to $[\partial^l \lambda_2(\theta, \varphi_i)]/(\partial \theta^l) = 0$, where l is an integer equal to or greater than 1. Using Taylor expansion near the neighborhood of the boundaries, one obtains

$$\frac{\partial \lambda_2(\theta, \varphi)}{\partial \theta} \approx \delta \varphi \frac{\partial^2 \lambda_2(\theta, \varphi_i)}{\partial \theta \partial \varphi}, \quad (31)$$

where $\delta \varphi = \varphi - \varphi_i$. The above approximation leads to

$$\lambda_2(\theta, \varphi) \approx \delta \varphi \frac{\partial^2 \lambda_2(\theta, \varphi_i)}{\partial \theta \partial \varphi} (\theta - \theta_0) + \Psi(\varphi), \quad (32)$$

where θ_0 is an initial point, $\Psi(\varphi)$ is a function of φ , and the overbar represents an average over the region from θ_0 to θ . Because $\lambda_2(\theta, \varphi_i) = 0$, $\Psi(\varphi)$ is also on the order of $\delta \varphi$. Taking the derivative of (32) with respect to φ gives

$$\frac{\partial \lambda_2(\theta, \varphi)}{\partial \varphi} \approx \frac{\partial^2 \lambda_2(\theta, \varphi_i)}{\partial \theta \partial \varphi} (\theta - \theta_0) + \frac{\partial \Psi(\varphi)}{\partial \varphi} \quad (33)$$

Comparing (31) with (33), because $(\theta - \theta_0)$ is not necessarily small (order of 1), it is seen that the amplitude of $\partial \lambda_2 / \partial \theta$ is an order of $\delta \varphi$ smaller than $\partial \lambda_2 / \partial \varphi$ near the neighborhood of the latitudinal boundaries. Therefore, in the second mass conservation scheme, the zonal wind correction is an order of $\delta \varphi$ smaller than the meridional wind correction near the latitudinal boundaries. This analysis can be easily extended to the whole lat-

itudinal region as long as $\delta \varphi$ is small. The latitudinal region used in the current wind retrievals are from 50° to 76°S, so the maximum value of $\delta \varphi$ is approximately 0.22. From Table 2, the calculated maximum and average differences between \tilde{v} and v_{c2} at 54°S are 3.09 m s⁻¹ and 1.33 m s⁻¹ for January and 4.46 m s⁻¹ and 1.55 m s⁻¹ for July. These values lead to an estimated zonal wind correction on the order of 0.6 to 0.9 m s⁻¹ for the maximum difference and 0.2 to 0.3 m s⁻¹ for the average difference. These values are close to the actually computed differences between \tilde{u} and u_{c2} .

Based on the previous analysis, it is found that \tilde{u} and u_{c2} are essentially identical winds. Because of this, the wave structure in Fig. 9 reflects the behavior of the correction term $\partial \lambda_1 / \partial \theta$. Because there is no latitudinal boundary restriction on $\partial \lambda_1 / \partial \theta$, it yields a larger correction to \tilde{u} . This wave structure is added to the \tilde{u} field and causes differences in the wave amplitudes and phases between u_{c1} and u_{c2} . For instance, Fourier analyses of 500-hPa wind fields indicate that for January, u_{c1} has a total variance of 13.2 m² s⁻² and wavenumber 1 variance of 6.8 m² s⁻², which are similar to the ECMWF and NCEP–NCAR reanalysis values. However, \tilde{u} and u_{c2} have total variances of only 4.6 m² s⁻² and a negligible wavenumber 1 variance of 0.7 m² s⁻².

The previous analysis illustrates significant differences between the two methods. The second method is essentially a boundary value problem—its zonal wind is strongly constrained by the latitudinal boundary condition. In contrast, the first method does not require the latitudinal boundary conditions. However, the procedure

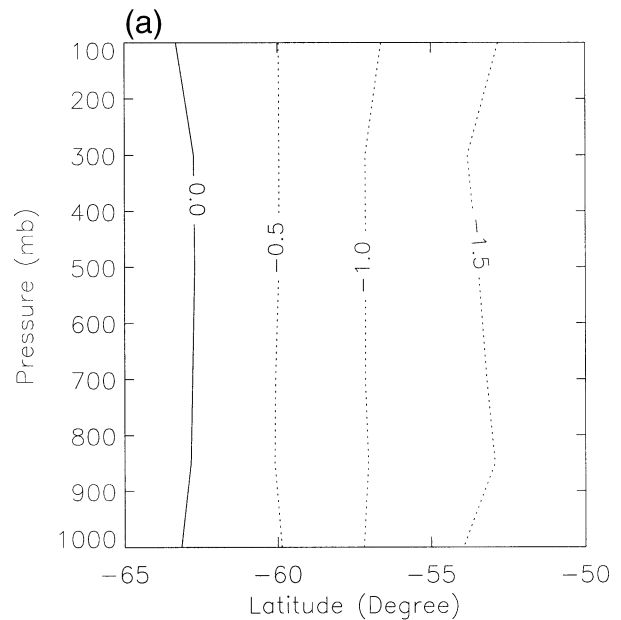


FIG. 4. Same as in Fig. 2 except for the monthly and zonally averaged meridional wind. (a) \tilde{v} ; (b) v_{c1} ; (c) v_{c2} ; (d) ECMWF reanalysis; (e) NCEP–NCAR reanalysis; (f) $v_{c1} - \text{ECMWF}$; (g) $v_{c1} - \text{NCEP–NCAR}$. Contour intervals are 0.5 m s⁻¹ for (a)–(e), and 0.25 m s⁻¹ for (f) and (g).

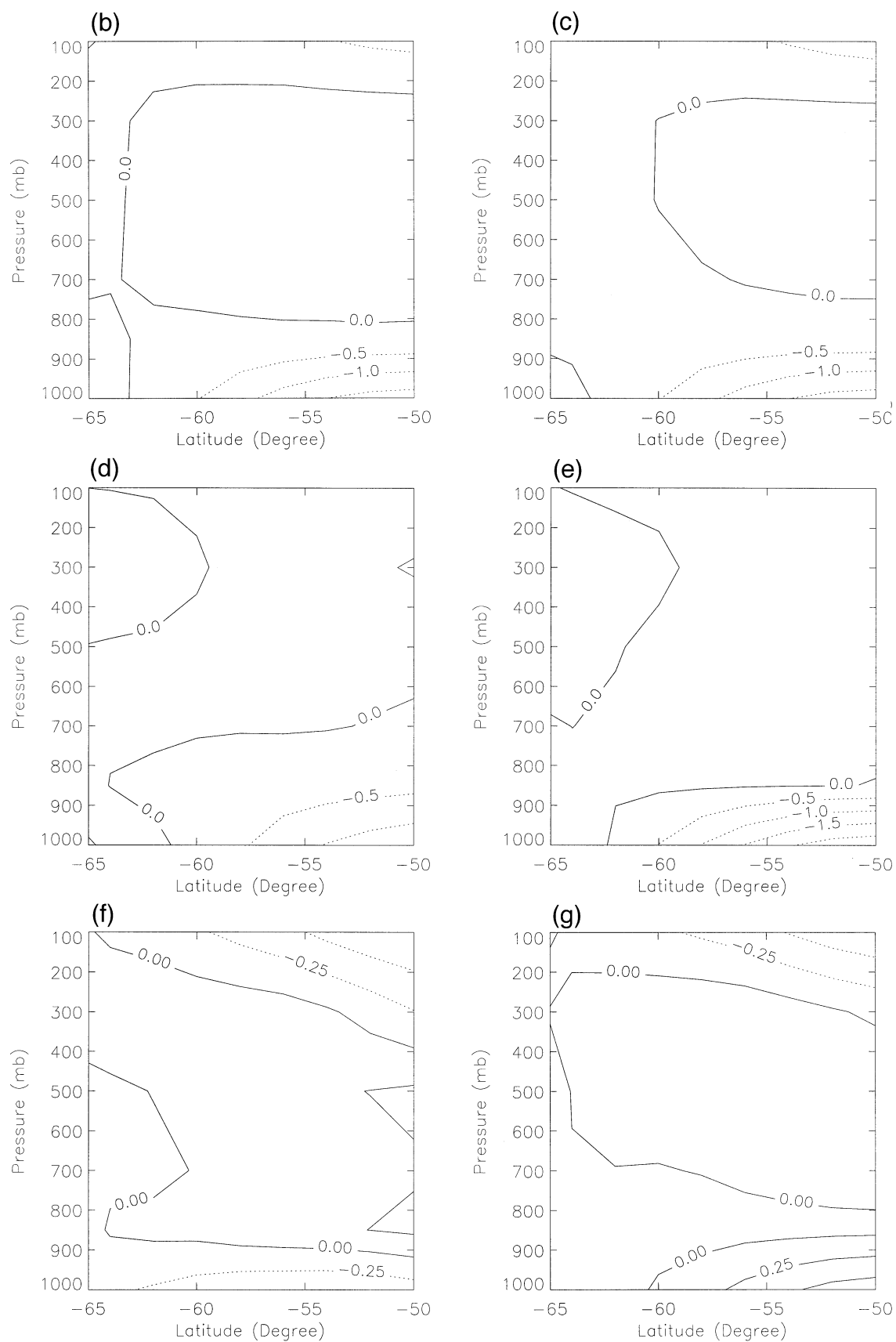


FIG. 4. (Continued)

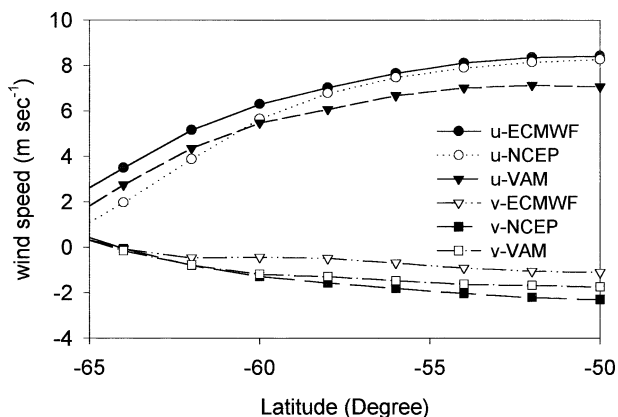


FIG. 5. Zonal-mean surface winds of the zonal, u , and meridional, v , components for Jul 1988.

requires obtaining the meridional wind first and then secondly, the zonal component. Any meridional wind input can force the zonal wind to satisfy the mass conservation (5), but not all inputs give reasonable zonal winds. Errors in the input meridional wind are linearly transferred to the zonal component. In particular, assuming an error of $\Delta v_k = \delta v \cos \theta$ [which must satisfy the mass flux conservation (10)] is introduced into the input meridional wind, where δv is a constant, then the zonal wind error is found to be $\Delta u_k = (f_k \sum_{k=0}^N f_k) / (\sum_{k=1}^N f_k f_k) \delta v \sin \varphi \sin \theta$, which is in the same order as the meridional wind error. Therefore, the meridional wind must be accurate or it will corrupt the zonal wind. For example, \bar{v} should not be used as the input for the zonal wind estimation, because it compares poorly with radiosonde observations and does not have a reasonable general circulation structure. ZVW01 have shown that the meridional wind profiles obtained from (11) compares reasonably well with limited raob observations and its atmospheric general circulation structure is comparable with the ECMWF and NCEP–NCAR reanalyses. Their results suggest that v_{c1} is a good starting point for deriving the zonal wind.

Another difference between the two methods is that the first method satisfies both constraints (5) and (10), while the second satisfies (5) and its zonal integral $\partial / \partial \varphi \int_0^{2\pi} \sum_{k=0}^N f_k v_k \cos \varphi d\theta = 0$. In order for the meridional

wind to satisfy (10), the model atmosphere must include the poles or set $v = 0$ at the latitudinal boundaries. The wind retrievals in this study are performed over the region from 50° to 76° S and no latitudinal boundary conditions are required for the meridional winds. Therefore, Eq. (10) is not automatically satisfied by the second method. For instance, the actually calculated zonally and vertically averaged meridional wind for the second method is on the order of 0.5 m s^{-1} . This is 2 orders of magnitude larger than the value estimated by Oort and Peixóto (1983). To eliminate this problem, one can explicitly add (10) as another constraint in the variational formalism of the second method, so the retrieved meridional wind also satisfies (10). However, the retrieved zonal wind would still be very close to \bar{u} due to the latitudinal boundary restrictions of the Lagrange multiplier as demonstrated by (31) through (33).

Though different, both methods yield reasonable atmospheric general circulation structure. Therefore, their validity for climate studies can only be assessed through validation against real observations such as radiosonde measurements.

6. Comparison at Macquarie Island

To further assess the validity of the two mass conservation methods, the satellite winds are compared with the twice-daily wind observations at Macquarie Island, Tasmania (54.5° S, 158.9° E) for 1988. ZVW01 indicated that the 1988 annual-mean surface pressure at Macquarie Island was 997 hPa with a standard deviation of 5 hPa. This is very close to the 1000-hPa surface pressure assumption in the retrieval algorithm. Therefore, Macquarie Island is a fairly ideal station to test the performance of the satellite algorithm.

a. Zonal wind

Table 3 lists the statistics of the comparisons between the raob zonal winds and the satellite winds. The satellite winds at Macquarie Island were obtained by interpolating the values from the four surrounding grid points. Table 3 shows that the comparison is most favorable at the surface where the satellite wind is taken to be the VAM wind. At the surface, the correlation between the satellite and raob winds is 0.89, the root-mean-square (rms) error is 2.6 m s^{-1} , and the bias is 0.76 m s^{-1} . Atlas et al. (1996) indicated that the VAM surface wind speed has a rms error $< 2.4 \text{ m s}^{-1}$ and bias within $\pm 0.5 \text{ m s}^{-1}$ of

TABLE 1a. Avg and max differences between different zonal wind fields at 54° S for Jan 1988. The upper-right side above the diagonal line of zeros is the avg difference between the two corresponding winds indicated by the column and row titles. The lower-left side below the diagonal line of zeros is the max difference between the two corresponding winds. Units are m s^{-1} .

	u_{ecmwf}	u_{ncep}	\bar{u}	u_{c1}	u_{c2}
u_{ecmwf}	0	0.82	2.93	2.91	2.90
u_{ncep}	3.73	0	2.49	2.37	2.45
\bar{u}	10.04	10.17	0	1.10	0.17
u_{c1}	9.13	9.14	3.65	0	1.04
u_{c2}	9.82	9.86	0.61	3.21	0

TABLE 1b. Same as in Table 1a except for Jul 1998.

	u_{ecmwf}	u_{ncep}	\bar{u}	u_{c1}	u_{c2}
u_{ecmwf}	0	0.98	2.43	2.96	2.39
u_{ncep}	4.06	0	2.41	3.31	2.39
\bar{u}	9.00	9.45	0	2.79	0.25
u_{c1}	9.63	10.55	7.18	0	2.65
u_{c2}	8.76	9.21	0.72	6.71	0

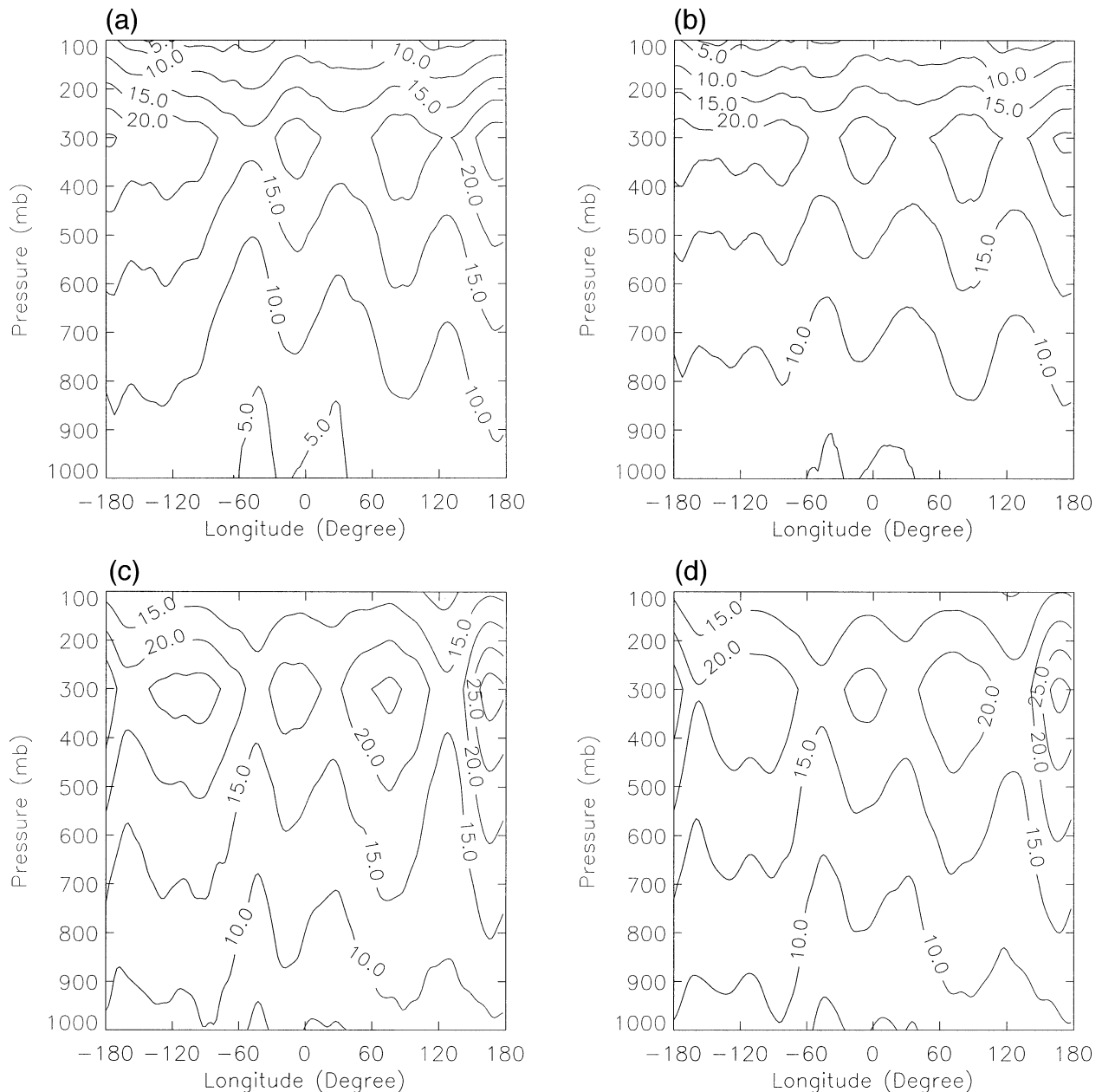


FIG. 6. Longitude–altitude cross sections of the monthly mean zonal winds at 54°S for Jan 1988. (a) u_{c1} ; (b) u_{c2} ; (c) ECMWF reanalysis; (d) NCEP–NCAR reanalysis. Satellite data are smoothed using a five-point running mean. Contour intervals are 5 m s^{-1} .

buoy winds over most of the tropical and Northern Hemispheric oceans. The rms error and bias at Macquarie Island are consistent with their results.

From Table 3, it is seen that the differences between the raob wind and \bar{u} are similar to the differences between the raob wind and u_{c2} . This again shows that \bar{u} is very similar to u_{c2} . Above the surface, the annual-mean \bar{u} has a typical bias of -3.5 to -4.5 m s^{-1} compared to the raob data and the bias of u_{c2} is nearly the same as \bar{u} . These biases are larger compared to the VAM surface wind. This vertical inhomogeneity in the

bias would most likely yield unrealistic vertical wind shear near the planetary boundary layer (assuming the raob data are the truth). Francis and Cermak (2001) found similar biases between the ECMWF (as well as NCEP–NCAR) reanalyses and independent radiosonde observations (except that it was positive—reanalysis westerly winds were too strong) in the middle and upper troposphere over the Arctic. In contrast, except at 100 hPa, u_{c1} has a bias of approximately -1 m s^{-1} throughout the troposphere. This bias is close to the bias range of the VAM surface wind. The surface wind

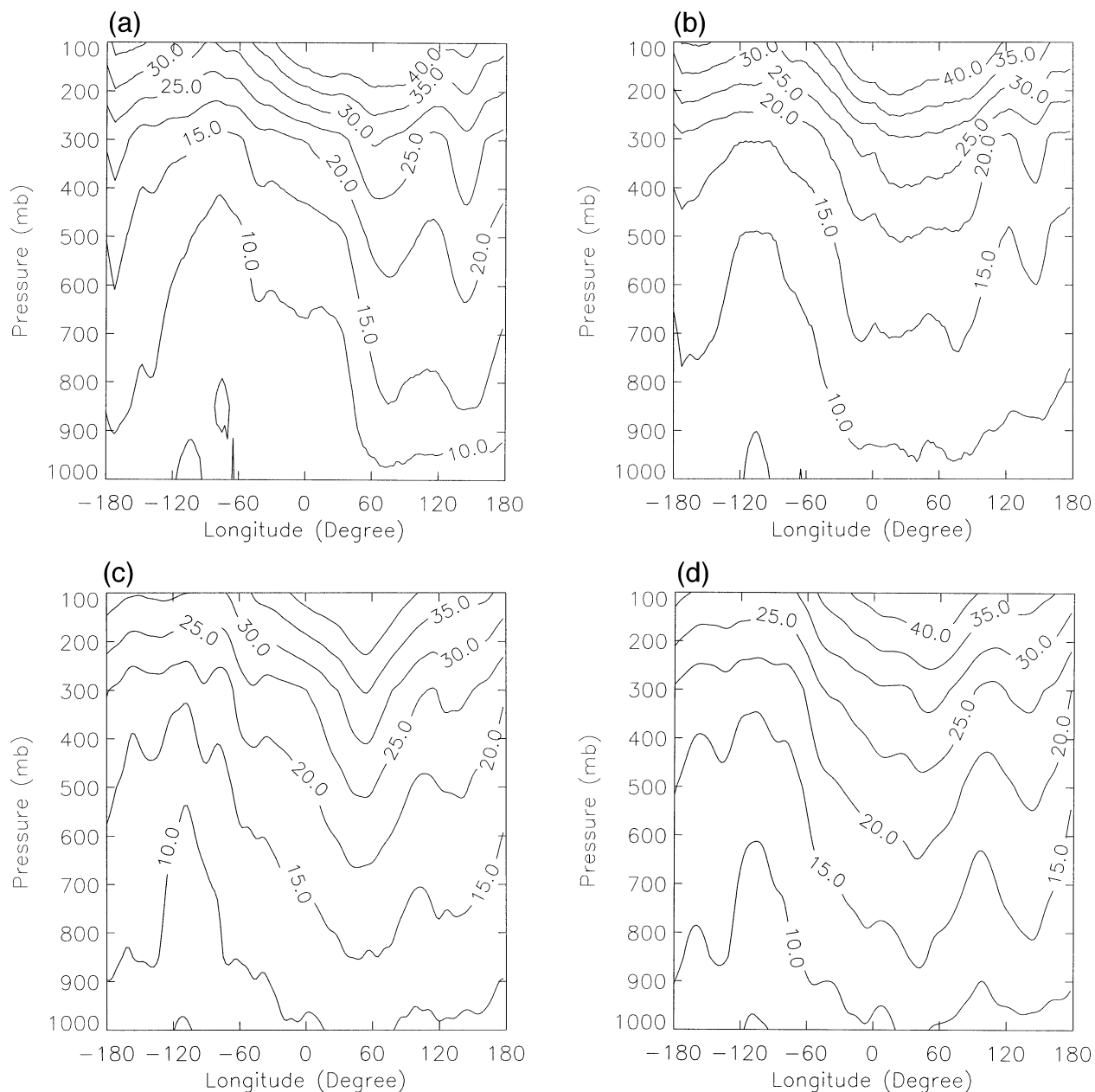


FIG. 7. Same as in Fig. 6 except for Jul 1988. (a) u_{e1} ; (b) u_{e2} ; (c) ECMWF reanalysis; (d) NCEP-NCAR reanalysis. Contour intervals are 5 m s^{-1} .

bias represents the lower limit on the upper-level wind, since the upper-level wind is directly added to the surface wind.

For instantaneous winds, both u_{e1} and u_{e2} yield rms errors comparable to the standard deviations of the raob wind. This is much larger than the WMO (1996) required accuracy (the required rms accuracy is at least 5 m s^{-1} in the troposphere and 10 m s^{-1} at the tropopause). There are many reasons for the large rms errors. Some of these are the spatial and temporal differences

between the satellite and raob data. In particular, the TOVS data are spatial- and temporal-averaged data with a spatial resolution of $1^\circ \times 1^\circ$ and time period of 24 h, while the radiosonde measurements are point data. Kitchen (1987) showed that observations separated in space and time would result in large errors when those observations are compared with each other. For instance, two wind observations in the Northern Hemispheric midlatitudes separated by 12 h at the same location would have rms errors varying from 6 m s^{-1} near the

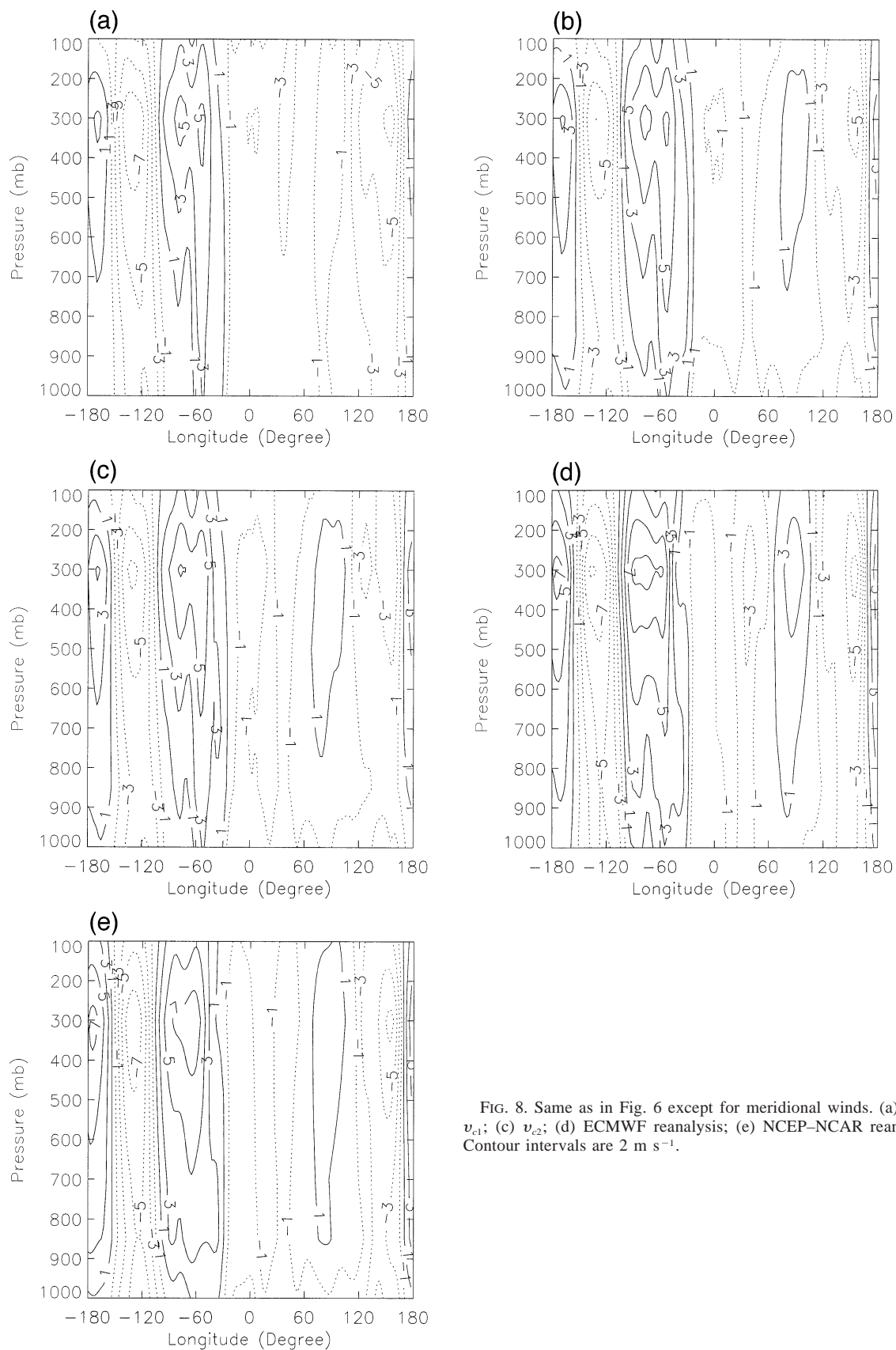


FIG. 8. Same as in Fig. 6 except for meridional winds. (a) \tilde{u} ; (b) v_{e1} ; (c) v_{e2} ; (d) ECMWF reanalysis; (e) NCEP-NCAR reanalysis. Contour intervals are 2 m s⁻¹.

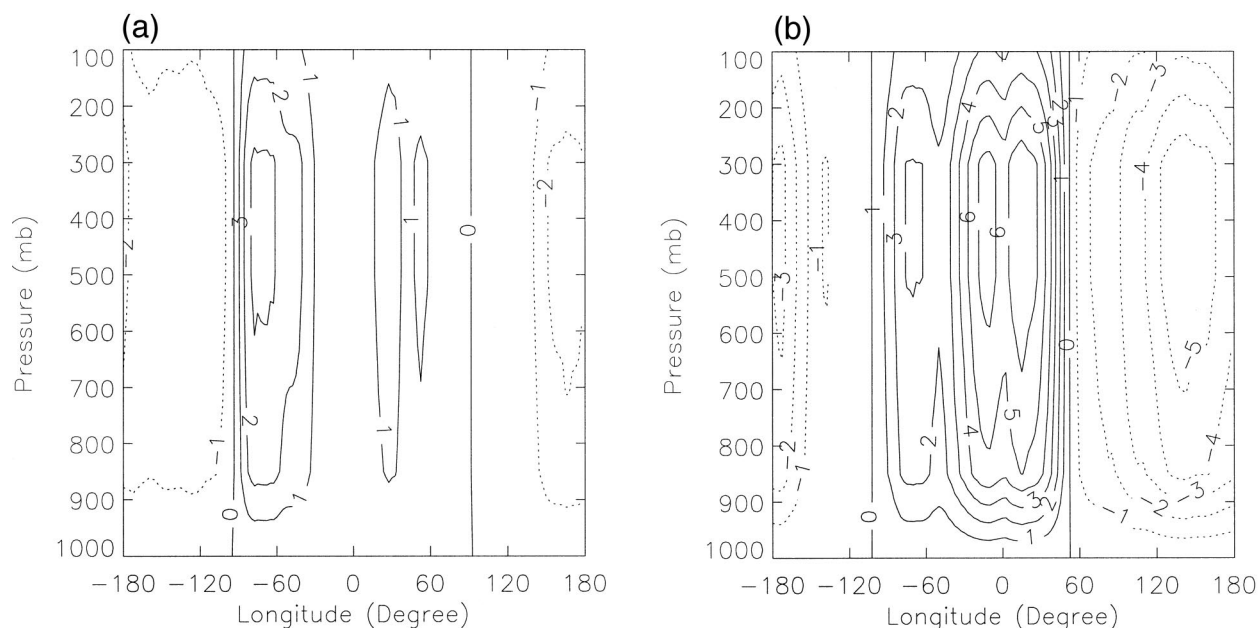


FIG. 9. Differences of the monthly mean zonal winds between the two mass conservation schemes at 54°S. (a) $u_{c2} - u_{c1}$, Jan 1988; (b) $u_{c2} - u_{c1}$, Jul 1988. Data are smoothed using a five-point running mean. Contour intervals are 1 m s⁻¹.

surface to 16 m s⁻¹ near 300 hPa (Kitchen 1987). Considering these factors, the rms errors in Table 3 appear to be acceptable.

Table 3 also shows that the rms errors of u_{c2} are about 1.5 m s⁻¹ smaller than u_{c1} from 850 to 300 hPa. The rms error largely measures the scatter between the satellite winds and the raob winds, therefore, they provide information on how closely the satellite portrays the eddy wind field. If we define $u' = u - \bar{u}$ as the eddy wind, where the overbar represents the time average and the prime denotes the deviation from the time average, and use $Y = \sqrt{[u'(\text{raob}) - u'(\text{sat})]^2}$ to measure the closeness between the satellite eddy wind and the raob eddy wind, then

$$Y = \sqrt{[u(\text{raob}) - \bar{u}(\text{raob}) - u(\text{sat}) + \bar{u}(\text{sat})]^2} \\ = \sqrt{\text{rms}^2(\text{raob, sat}) - \text{bias}^2(\text{raob, sat})} \quad (34)$$

The smaller rms error and larger bias between u_{c2} and the raob wind lead to a Y value about 2 m s⁻¹ smaller than the Y value of u_{c1} in the lower troposphere. This suggests that the eddy wind from u_{c2} is better than u_{c1} .

The above comparisons demonstrate that u_{c1} and u_{c2} behave quite differently— u_{c1} has smaller biases while

u_{c2} has better instantaneous winds. Since it is essential for the biases to be minimal for climate applications, u_{c1} appears to be more suitable for climate studies. In order for u_{c2} to be suitable for climate studies, its large bias must be removed or reduced. Since u_{c2} is nearly the same as \tilde{u} , improvements in u_{c2} must be made by improving \tilde{u} . As seen from its construction, \tilde{u} lacks ageostrophic dynamics—the only ageostrophic component comes from the surface. However, other ageostrophic winds introduced by the geostrophic-momentum approximation or the ageostrophic acceleration itself could be very important in certain situations (e.g., Shapiro and Kennedy 1981). Including other dynamic processes might be one way of reducing the bias in \tilde{u} .

b. Meridional wind

ZVW01 have compared \tilde{v} and v_{c1} with the radiosonde observations at Macquarie Island in detail. Here, their results, along with the comparisons of v_{c2} , are summarized in Table 4. As noted in ZVW01, the most significant improvement for v_{c1} over \tilde{v} is in the annual-mean wind field. The annual-mean v_{c1} agrees with the raob wind to within 27%, while the annual-mean \tilde{v} is

TABLE 2a. Same as in Table 1a except for the meridional wind.

	v_{ecmwf}	v_{ncep}	\tilde{v}	v_{c1}	v_{c2}
v_{ecmwf}	0	0.61	1.52	1.04	1.10
v_{ncep}	3.02	0	1.51	0.87	0.90
\tilde{v}	5.21	5.21	0	1.42	1.33
v_{c1}	3.54	3.54	1.79	0	0.39
v_{c2}	4.34	3.93	3.09	1.30	0

TABLE 2b. Same as in Table 2a except for Jul 1998.

	v_{ecmwf}	v_{ncep}	\tilde{v}	v_{c1}	v_{c2}
v_{ecmwf}	0	0.65	1.63	1.00	1.35
v_{ncep}	2.38	0	1.59	0.94	1.16
\tilde{v}	5.52	6.01	0	1.54	1.55
v_{c1}	3.97	4.96	1.95	0	0.92
v_{c2}	4.66	4.48	4.46	2.51	0

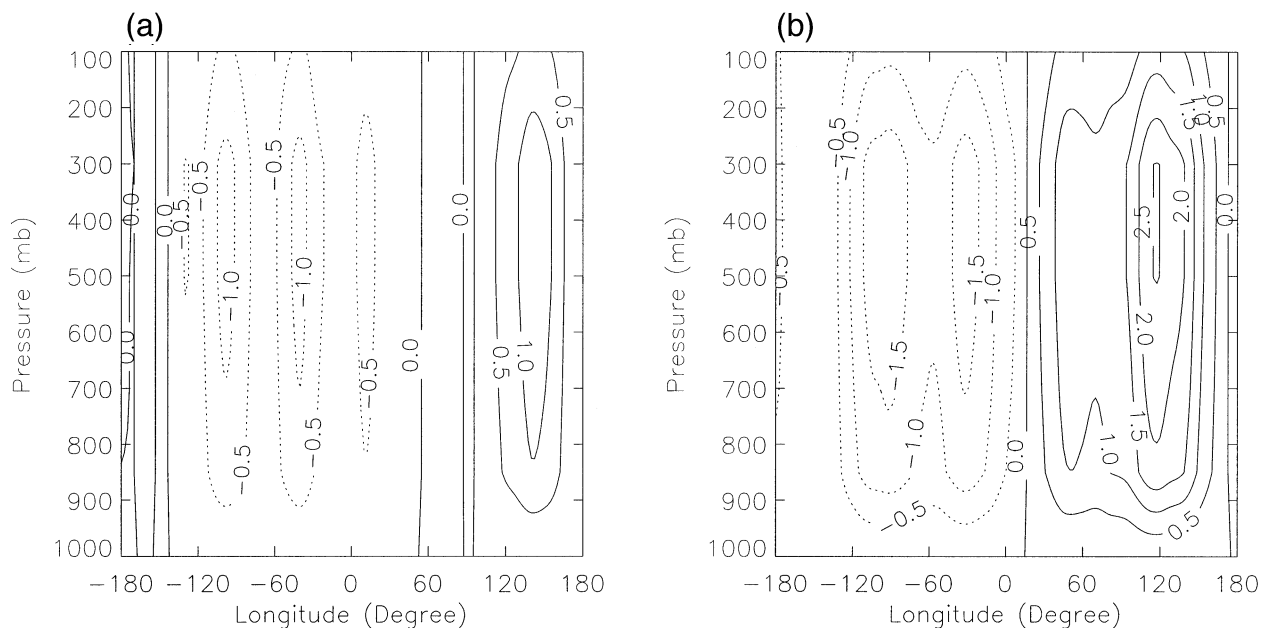


FIG. 10. Same as in Fig. 9 except for the meridional wind. (a) $v_{c2} - v_{c1}$, Jan 1988; (b) $v_{c2} - v_{c1}$, Jul 1988. Contour intervals are 0.5 m s^{-1} .

typically 100% stronger than the raob mean winds. Most of the statistics, including the rms errors, between v_{c2} and the raob wind are similar to the statistics between v_{c1} and the raob wind. This is consistent with their structural comparisons in the earlier sections. However, the annual-mean v_{c2} appears to be 50% to 70% weaker in the troposphere than the raob annual mean, resulting in a larger bias compared to v_{c1} . This is probably because v_{c2} does not satisfy the theoretical constraint Eq. (10), as mentioned in earlier sections.

7. Summary

The thermal wind relationship plus a variational technique for conserving mass has been developed in this

study to retrieve the three-dimensional horizontal wind field from satellite temperature soundings and the surface wind field over the middle- and high-latitude oceans. In this technique the thermal wind derived from the satellite temperature profiles plus the surface wind is used as a first-guess wind profile, then a Lagrange multiplier is introduced in a variational formalism to constrain the first-guess wind to conserve mass. Two mass conservation schemes have been proposed. One is to use the meridional mass transport conservation equation as a constraint to retrieve the meridional wind first, and then the vertically integrated mass conservation equation is used to infer the zonal wind. The meridional and zonal winds are obtained sequentially in this ap-

TABLE 3. Statistics between raob and satellite-derived zonal winds at Macquarie Island for 1998.

Height	1000 hPa	850 hPa	700 hPa	500 hPa	300 hPa	100 hPa
Number of points	523	536	536	532	510	409
Raob mean (m s^{-1})	6.02	13.16	16.13	21.68	28.11	24.87
\bar{u} mean (m s^{-1})	6.77	9.51	12.54	17.45	23.95	20.34
u_{c1} mean (m s^{-1})	6.77	11.83	15.16	20.43	27.20	22.06
u_{c2} mean (m s^{-1})	6.77	9.80	12.91	17.86	24.40	20.59
Raob std (m s^{-1})	5.48	9.05	9.81	12.71	16.58	12.60
\bar{u} std (m s^{-1})	4.98	5.60	7.44	10.83	13.77	17.72
u_{c1} std (m s^{-1})	4.98	8.80	10.24	13.42	15.84	17.65
u_{c2} std (m s^{-1})	4.98	5.46	7.19	10.52	13.43	17.82
Correlation (raob, \bar{u})	0.89	0.78	0.66	0.64	0.63	0.72
Correlation (raob, u_{c1})	0.89	0.60	0.57	0.58	0.61	0.72
Correlation (raob, u_{c2})	0.89	0.80	0.69	0.68	0.69	0.73
Rms (raob, \bar{u}) (m s^{-1})	2.62	6.91	8.25	10.96	13.94	13.13
Rms (raob, u_{c1}) (m s^{-1})	2.62	8.14	9.31	12.00	14.29	12.51
Rms (raob, u_{c2}) (m s^{-1})	2.62	6.67	7.78	10.31	13.19	12.94
Bias ($\bar{u} - \text{raob}$) (m s^{-1})	0.76	-3.67	-3.61	-4.23	-4.16	-4.52
Bias ($u_{c1} - \text{raob}$) (m s^{-1})	0.76	-1.32	-0.96	-1.20	-0.91	-2.88
Bias ($u_{c2} - \text{raob}$) (m s^{-1})	0.76	-3.41	-3.24	-3.82	-3.71	-4.32

TABLE 4. Same as in Table 3 except for the meridional winds.

Height	1000 hPa	850 hPa	700 hPa	500 hPa	300 hPa	100 hPa
Number of points	523	539	538	532	510	409
Raob mean (m s^{-1})	-2.26	-1.28	-1.24	-1.08	-2.42	-1.02
\bar{v} mean (m s^{-1})	-2.26	-2.41	-2.64	-3.00	-3.90	-2.44
v_{c1} mean (m s^{-1})	-2.26	-0.94	-0.93	-1.04	-1.83	-1.62
v_{c2} mean (m s^{-1})	-2.26	-0.46	-0.38	-0.38	-1.15	-1.21
Raob std (m s^{-1})	5.69	9.37	10.88	14.25	18.70	9.15
\bar{v} std (m s^{-1})	5.66	6.30	8.18	11.86	14.68	9.62
v_{c1} std (m s^{-1})	5.66	6.01	7.65	10.95	13.85	9.06
v_{c2} std (m s^{-1})	5.66	5.73	7.02	10.08	12.88	8.76
Correlation (raob, \bar{v})	0.87	0.82	0.79	0.77	0.77	0.55
Correlation (raob, v_{c1})	0.87	0.84	0.81	0.79	0.78	0.60
Correlation (raob, v_{c2})	0.87	0.84	0.83	0.83	0.82	0.62
Rms (raob, \bar{v}) (m s^{-1})	2.89	5.63	6.88	9.29	11.29	9.05
Rms (raob, v_{c1}) (m s^{-1})	2.89	5.47	6.52	8.78	11.65	8.17
Rms (raob, v_{c2}) (m s^{-1})	2.89	5.61	6.46	8.15	11.12	7.79
Bias (\bar{v} - raob) (m s^{-1})	0.0	-1.13	-1.41	-1.92	-1.48	-1.42
Bias (v_{c1} - raob) (m s^{-1})	0.0	0.33	0.31	0.05	0.55	-0.60
Bias (v_{c2} - raob) (m s^{-1})	0.0	0.82	0.86	0.71	1.23	-0.20

proach. The second scheme is to use the vertically integrated mass conservation as a constraint to retrieve the zonal and meridional winds simultaneously from the first-guess wind. Comparisons of the two wind fields with the ECMWF and NCEP–NCAR reanalyses over the Southern Ocean and radiosonde observations at Macquarie Island, Tasmania lead to the following conclusions:

- 1) Both mass conservation schemes result in significant improvements in the monthly mean meridional wind compared to \bar{v} . Both v_{c1} and v_{c2} have atmospheric general circulation structure similar to the ECMWF and NCEP–NCAR reanalysis winds. However, v_{c1} satisfies more physical constraints than v_{c2} and it has a smaller bias than v_{c2} compared to the radiosonde observations. In addition, quantitative comparisons suggest that v_{c1} is closer to the reanalysis winds than v_{c2} (Table 2).
- 2) Because of the restriction of the latitudinal boundary conditions, the second mass conservation scheme results in u_{c2} being essentially identical to \bar{u} . The first-guess wind \bar{u} has an annual-mean bias of approximately -4 m s^{-1} at Macquarie Island. The first method reduces this bias to approximately -1 m s^{-1} , while u_{c2} has approximately the same bias as \bar{u} . In contrast, \bar{u} and u_{c2} have smaller rms errors than u_{c1} compared to radiosonde data.
- 3) Moreover, \bar{u} , u_{c1} , and u_{c2} all have the same zonal-mean structure and it is similar to the ECMWF and NCEP–NCAR reanalyses. However, there is a phase shift between u_{c1} and u_{c2} in the zonal direction, caused by the zonal wave structure in the correction term, $\partial\lambda_1/\partial\theta$. This wave structure leads to differences of u_{c1} and u_{c2} in their zonal wavenumber spectra.
- 4) The overall comparisons suggest that the monthly mean u_{c1} and v_{c1} are probably more suitable for climate studies because their biases are small.

These conclusions are based on the results over the Southern Ocean and limited radiosonde comparisons. More validations using radiosonde observations are needed to further assess the validity of each method. In particular, it would be interesting to know whether similar results can be obtained over the Northern Hemispheric oceans.

Acknowledgments. Joel Susskind and Paul Piraino provided the TOVS Path A data. Robert Atlas and Joe Ardizzone provided the SSM/I-based surface wind fields. The ECMWF analysis and reanalysis data are supplied by NCAR. Yuejian Zhu provided the NCEP–NCAR reanalysis data. Their efforts in producing these datasets are greatly appreciated. We also appreciate Dr. Milijia Zupanski and Dr. Peitao Peng for their comments and discussions on solving the Euler–Lagrange equations. Comments from the three anonymous reviewers greatly helped to improve the manuscript. This study was supported by NASA Grant W18,795.

REFERENCES

- Atlas, R., R. N. Hoffman, S. C. Bloom, J. C. Jusem, and J. Ardizzone, 1996: A multi-year global surface wind velocity dataset using SSM/I wind observations. *Bull. Amer. Meteor. Soc.*, **77**, 869–882.
- Boutin, J., and J. Etcheto, 1996: Consistency of Geosat, SSM/I, and ERS-1 global surface wind speeds—Comparison with in situ data. *J. Atmos. Oceanic Technol.*, **13**, 183–197.
- Bromwich, D. H., F. M. Robasky, R. I. Cullather, and M. L. Van Woert, 1995: The atmospheric hydrologic cycle over the Southern Ocean and Antarctica from operational numerical analyses. *Mon. Wea. Rev.*, **123**, 3518–3538.
- , A. N. Rogers, P. Källberg, R. I. Cullather, J. W. C. White, and K. J. Kreutz, 2000: ECMWF analyses and reanalyses depiction of ENSO signal in Antarctic precipitation. *J. Climate*, **13**, 1406–1420.
- Cullather, R. I., D. H. Bromwich, and M. L. Van Woert, 1996: Interannual

- variations in Antarctic precipitation related to El Niño–Southern Oscillation. *J. Geophys. Res.*, **101**, 19 109–19 118.
- , —, and M. C. Serreze, 2000: The atmospheric hydrologic cycle over the Arctic basin from reanalyses. Part I: Comparison with observations and previous studies. *J. Climate*, **13**, 923–937.
- Daley, R., 1991: *Atmospheric Data Analysis*. Cambridge University Press, 457 pp.
- Francis, J. A., and R. Cermak, 2001: Satellite-observed changes in energy advection within the arctic. Preprints, *Sixth Conf. on Polar Meteorology and Oceanography*, San Diego, CA, Amer. Meteor. Soc., 45–48.
- Gates, W. L., and Coauthors, 1999: An overview of the results of the Atmospheric Model Intercomparison Project (AMIP I). *Bull. Amer. Meteor. Soc.*, **80**, 29–55.
- Genthon, C., and G. Krinner, 1998: Convergence and disposal of energy and moisture on the Antarctic polar cap from ECMWF reanalyses and forecasts. *J. Climate*, **11**, 1703–1716.
- Gibson, R., P. Kallberg, S. Uppala, A. Hernandez, A. Nomura, and E. Serrano, 1997: ECMWF re-analysis project report series: 1. ERA description. European Centre for Medium-Range Weather Forecasts, 72 pp.
- Green, J. S. A., 1970: Transfer properties of the large-scale eddies and the general circulation of the atmosphere. *Quart. J. Roy. Meteor. Soc.*, **96**, 157–185.
- Groves, D. G., 2001: The moisture budget of the Arctic atmosphere from TOVS satellite data. M. S. thesis, Dept. of Atmospheric Sciences, University of Washington, Seattle, 93 pp.
- Gruber, A., and J. J. O'Brien, 1968: An objective analysis of wind data for energy budget studies. *J. Appl. Meteor.*, **7**, 333–338.
- Haltiner, G. J., and R. T. Williams, 1980: *Numerical Prediction and Dynamic Meteorology*. John Wiley and Sons, 477 pp.
- Held, I. M., and A. Y. Hou, 1980: Nonlinear axially symmetric circulations in a nearly inviscid atmosphere. *J. Atmos. Sci.*, **37**, 515–533.
- Kalnay, E., and Coauthors, 1996: The NCEP/NCAR 40-Year Reanalysis Project. *Bull. Amer. Meteor. Soc.*, **77**, 437–471.
- Kasahara, A., 1974: Various vertical coordinate systems used for numerical weather prediction. *Mon. Wea. Rev.*, **102**, 509–522.
- Kistler, R., and Coauthors, 2001: The NCEP–NCAR 50-Year Reanalysis: Monthly means CD-ROM and documentation. *Bull. Amer. Meteor. Soc.*, **82**, 247–267.
- Kitchen, M., 1987: Representativeness errors for radiosonde observations. *Radiosonde Data Quality and Monitoring*, ECMWF/WMO Workshop, European Centre for Medium-Range Weather Forecasts, Reading, United Kingdom, 43–55.
- Lindzen, R. S., and H.-L. Kuo, 1969: A reliable method for the numerical integration of a large class of ordinary and partial differential equations. *Mon. Wea. Rev.*, **97**, 732–734.
- Lorenz, E. N., 1967: The nature and theory of the general circulation of the atmosphere. WMO Publ. 218, TP115, World Meteorological Organization, 161 pp.
- Oort, A. H., and J. P. Peixoto, 1983: Global angular momentum and energy balance requirements from observations. *Advances in Geophysics*, Vol. 25, Academic Press, 355–490.
- Peixoto, J. P., and A. H. Oort, 1992: *Physics of Climate*. American Institute of Physics, 520 pp.
- Sasaki, Y. K., P. S. Ray, J. S. Georss, and P. Soliz, 1979: Inconsistent finite differencing errors in the variational adjustment of horizontal wind components. *J. Meteor. Soc. Japan*, **57**, 88–92.
- Schmetz, J., K. Holmlund, J. Hoffman, B. Strauss, B. Mason, V. Gaertner, A. Koch, and L. Van De Berg, 1993: Operational cloud-motion winds from Meteosat infrared images. *J. Appl. Meteor.*, **32**, 1206–1225.
- Schneider, E. K., and R. S. Lindzen, 1977: Axially symmetric steady-state models of the basic state for instability and climate studies. Part I. Linearized calculations. *J. Atmos. Sci.*, **34**, 263–279.
- Shapiro, M. A., and P. J. Kennedy, 1981: Research aircraft measurements of jet stream geostrophic and ageostrophic winds. *J. Atmos. Sci.*, **38**, 2642–2652.
- Slonaker, R. L., and M. L. Van Woert, 1999: Atmospheric moisture transport across the Southern Ocean via satellite observations. *J. Geophys. Res.*, **104**, 9229–9249.
- Susskind, J., 1993: Water vapor and temperature. *Atlas of Satellite Observations Related to Global Change*, R. J. Gurney, J. L. Foster, and C. L. Parkinson, Eds., Cambridge University Press, 89–128.
- , and J. Pfaendner, 1989: Impact of Interactive Physical Retrievals NWP. Report on the Joint ECMWF/EUMETSAT Workshop on the Use of Satellite Data in Operational Weather Prediction: 1989–1993. Vol. 1, T. Hollingsworth, Ed., ECMWF, 245–270.
- , P. Piraino, L. Rokke, L. Iredell, and A. Mehta, 1997: Characteristics of the TOVS Path A dataset. *Bull. Amer. Meteor. Soc.*, **78**, 1449–1472.
- Van Loon, H., 1972: Wind in the Southern Hemisphere. *Meteorology of the Southern Hemisphere*, Meteor. Monogr., No. 35, Amer. Meteor. Soc., 87–99.
- Wang, M., and J. Paegle, 1996: Impact of analysis uncertainty upon regional atmospheric moisture flux. *J. Geophys. Res.*, **101**, 7291–7303.
- WMO, 1996: *Guide to Meteorological Instruments and Methods of Observation*. 6th ed. WMO-8, Secretariat of the World Meteorological Organization.
- Zou, C.-Z., and M. L. Van Woert, 2001: The role of conservation of mass in the satellite-derived poleward moisture transport over the Southern Oceans. *J. Climate*, **14**, 997–1016.